Spring 2019

Non-local Spin Valve Interferometer: Experimental Observation of Superconducting Spin Current and Spin Aharonov-Bohm Effect

Ning Lu

Non-local Spin Valve Interferometer: Experimental Observation of Superconducting Spin Current and Spin Aharonov-Bohm Effect

by

Ning Lu

Bachelor of Science
Hunan University 2005

Master of Science
Hunan University 2008

Submitted in Partial Fulfillment of the Requirements

for the Degree of Doctor of Philosophy in

Physics

College of Arts and Sciences

University of South Carolina

2019

Accepted by:

Scott Crittenden, Major Professor

Yaroslaw Bazaliy, Committee Member

Yanwen Wu, Committee Member

Andrew Greytak, Committee Member

Cheryl L. Addy, Vice Provost and Dean of the Graduate School

Acknowledgments

First, I would like to express my appreciation to my former advisor Prof. Richard Webb who not only trained me the experimental techniques with kindness and patience but also inspired and encouraged me to do independent and creative scientific research in Physics. His strong will power and optimistic attitude in front of surgeries encouraged me a lot. It is an enjoyment to work together with him, such as pushing liquid Nitrogen, maintaining the SEM, the PPMS and the liquefier. Thanks to the academic environment he built up, I could grow up slowly, design my own project and conquer the most difficult part of sample fabrication.

I would like to appreciate Pro. Scott Crittenden, my current advisor, for his very helpful and illuminating discussion on the physics of the experiment. He taught me how to learn and promote oneself from discussion of physics. He also helped me a lot on academic paper writing and written English.

I would like to thank Pro. Thomas Crawford for the help in the application of National High Magnetic Field Lab (NHMFL) and his support of making measurement in NHMFL in University of Florida. I would like to thank Pro. Yaroslaw Bazaliy, Pro. Yanwen Wu, Pro. Andrew Greytak, Pro. Richard Creswick and Pro. Brett Altstchul for all their helpful discussion on Physics and their support. I thank former and current group members in Dr. Webb's lab and in the USC nanocenter, including Dr. Bochen Zhong, Dr. Longfei Ye, Dr. Lei Wang, Mr. Ken Stepnenson, Ms. Sara FitzGerald, Mr. Rahman Mohtasebzadeh and Mr. Heath Smith for their help in the lab.

A portion of this work was performed at the National High Magnetic Field Labo-

ratory High B/T facility, which is supported by National Science Foundation Cooperative Agreement No. DMR- 1644779, the State of Florida, and the U.S. Department of Energy.

Finally, I would give my special thanks to my wife Kaimei Tang, my parents, my two kids Xiran Lu and Anna Lu and all the other family members. I appreciate for their supporting me, both spiritually and substantially, to pursue the truth and logic of the nature and science. It is their warm and endless support that made me able to walk longer in academic research.

Abstract

An electron interferometer was designed and fabricated via a normal metal (superconductor)/insulator/ferromagnet non-local lateral spin valve with a ring-shaped normal metal/insulator spacer, and spin current interference was observed. At 4.2 K, a very high spin signal of 200 mΩ was found in a device with 2 μm injector-detector distance and magnetic field swept parallel to the plane. With a perpendicular magnetic field sweep, a Hanle effect measurement showed both spin precession and h/e oscillation. Because of the non-adiabatic nature of the precessing spins at low fields as they traverse the normal metal ring, this is an experimental observation of Aharonov-Anandan's non-adiabatic geometric phase.

In addition, our observation of identical spin resistance for normal and superconducting Aluminum is inconsistent with theoretical predictions based on the quasiparticle picture. In this designed sample, at the injector region, it is actually a superconductor/ferromagnet/superconductor lateral Josephson junction. Such a lateral Josephson junction convert spin singlet Cooper pairs from Aluminum to the long range triplet components in ferromagnet with projection of $S_z = \pm 1$. Such long range triplet components could diffuse a long distance in ferromagnet bar which is shorter than 3μm. The spin current results in superconducting Aluminum not only suggested the singlet-triplet conversion in ferromagnet, but may also suggest a new phenomenon, that is the long range triplet correlation in ferromagnet may also reversely spread out into type I superconductor and exist for a short period of time in the superconductor and finally convert to singlet correlation due to exchange interaction and spin-orbital coupling. Such an unstable triplet correlation in Aluminum

could be detected in the non-local geometry. Although additional experimental work is needed to further confirm this supposition, our results might be the direct observation of superconducting spin current which was under experimental pursuit recently. The experimental results may also suggest a new research area, that is triplet-singlet conversion in type I superconductor.

Table of Contents

List of Figures

Chapter 1

Introduction: Spintronics

Spintronics is to utilize and manipulate the spin degree of freedom of electron in solid state devices. The fundamental research of spintronics includes spin generation, detection and spin transport in different electronic materials such as metal, semiconductor and superconductor[96, 39, 14]. To control spin, one either control the population and phase of the spin with ensemble of particles, or coherently manipulate a single spin or several spin system.

Spin generation could be realized through different ways of creating non-equilibrium spin population. One is optical way which uses circularly polarized photons to transfer the angular momenta to electrons[52]. Another way is electrical spin injection from a ferromagnetic material. Spin dependent density of states (DOS) for ferromagnetic metal (FM) and normal metal (NM) is shown in figure 1.1. Near Fermi level, where most transport property depends on density of states, the asymmetry of spin up and spin down allow FM to generate, manipulate and detect spin signal. Once spin polarized electric current is injected from FM to NM, the non-equilibrium spin accumulates in NM. Then spin starts to relax and bring the non-equilibrium spin accumulation back equilibrium. Currently several spin relaxation mechanisms are proposed, Elliott-Yafet mechanism, D'yakonov-Perel Mechanism Bir-Aronov-Pikus mechanism and Hyperfine-interaction mechanism[30, 93, 28, 18, 29]. Most mechanisms involve spin-orbit coupling in combination with momentum scattering to serve as the source of spin randomization. Spin detection mainly utilize the sensing of change in the signals originated from spin non-equilibrium in a system.

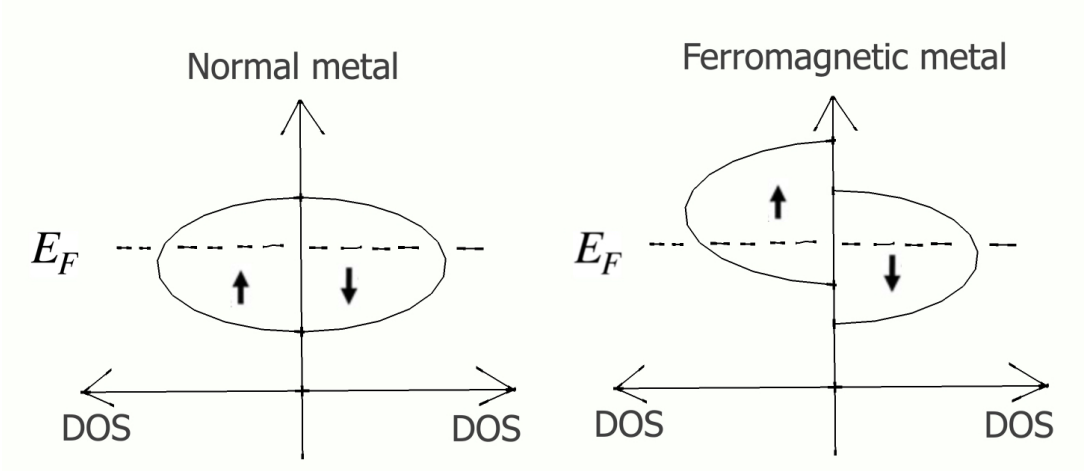

Figure 1.1 Density of States for spin up and spin down in NM and FM.

1.1 Giant Magnetoresistance and Tunneling Magnetoresistance

Currently, one of the most successful application of spintronics is in the hard disk drive for large volume information storage in modern information technology, in the form of giant magnetoresistance (GMR) and tunneling magnetoresistance (TMR)[24, 96, 31, 55, 83]. In 2007, Physics Nobel Prize was awarded to Albert Fert and Peter Grunberg for their discovery of GMR, which is a quantum mechanical magnetoresistance observed in multilayers composed of two FM layers and a NM layer between them. One is current in plane (CIP) in which the current flows along the superlattice layers. Another is current perpendicular to plane (CPP) in which the current passed perpendicular to the layers. The GMR value of CPP geometry is more than twice of that in CIP geometry. It is also easier to analyze the physics mechanism theoretically in CPP geometry which relates to the physics in magnetic tunnel junction. However, CIP geometry is used in most of the GMR geometry as it is easier to realize. Figure 1.2(a) shows the high giant magnetoresistance of about 80% from Fe/Cr superlattices prepared by molecular beam epitaxy [9]. Figure 1.2(b) shows the schematic diagram of the mechanism of CPP GMR. In parallel ferromagnets configu-

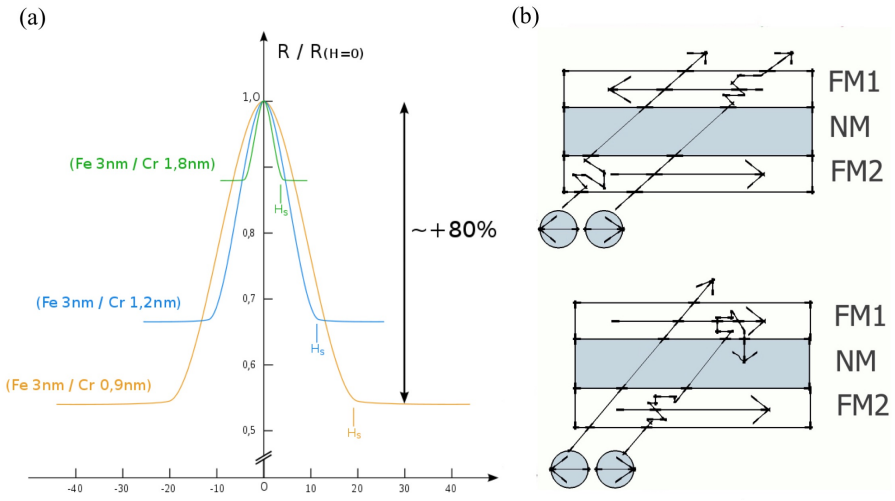

Figure 1.2 (a) GMR of Fe/Cr superlattices for CPP geometry [9], figure from Wikipedia. (b) Schematic diagram of CPP-GMR in FM/NM/FM multilayer[24]. If electron spin magnetic moment is anti-parallel with magnetization of a FM layer, it experiences larger resistance R_{large}; if spin magnetic moment is parallel with a FM layer, it experiences smaller resistance R_{small}. The two resistance stages for AP and P FM configurations are expressed as Eq. 1.1.

ration, electrons with one spin direction (parallel to the magnetization direction) can flow easily through both magnetic layers, so the resistance is lower. While in anti-parallel ferromagnets configuration, both spin up and spin down electrons experience same magnetic scattering, therefore the resistance is higher [31]. We can understand this by using resistance circuit representation for two magnetic configurations.

$$R_{AP} = \frac{R_{large} + R_{small}}{2}, R_P = \frac{R_{large} R_{small}}{R_{large} + R_{small}} \tag{1.1}$$

the The difference in resistance for parallel and anti-parallel configurations will be converted into proper digital voltage signals which can be used for information storage.

A step further is the Tunneling Magnetoresistance (TMR) observed in magnetic tunnel junction (MTJ) [55, 68, 69]. MTJ consists of two FM layers separated by a thin insulator which serves as tunnel junction. The insulator is often a few nanometers,

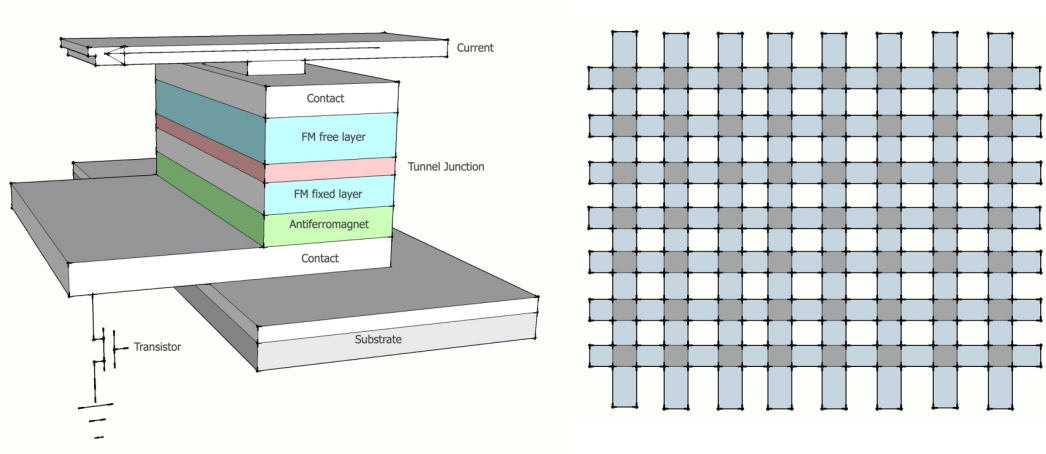

Figure 1.3 Two dimensional write selection with MRAM [4].

such that electrons can tunnel from one ferromagnet to the other. Early works used amorphous aluminum oxide as insulator and found relative resistance change $\frac{R_{ap}-R_p}{R_p}$ of 18% with iron FM layers and 11.8% with CoFe/Co FM layers at room temperature [68, 69]. The TMR value was enhanced a lot with the use of crystalline magnesium oxide (MgO) as tunnel barrier. Fe/MgO/Fe(CoFe) tunnel junctions show a TMR value of more than 200% at room temperature [95, 72, 21].

Even higher TMR value of 604% at 300 K and 1100% at 4.2 K were found in CoFeB/MgO/CoFeB junctions [48].

The current application of TMR is the read head of hard disk drive (HDD) in the information storage. Another application of MTJ is in magnetoresistive random access memory (MRAM). The proponents of MRAM believe that MRAM will finally become a kind of universal memory (as shown in figure 1.3)which can combine flash RAM and dynamic RAM which are existing memory technologies [4].

1.2 Non-local Spin Valve

Non-local spin valve (NLSV) is generally considered as an effective way to generate spin currents which only carry spin angular momenta, in contrary to the case in GMR,

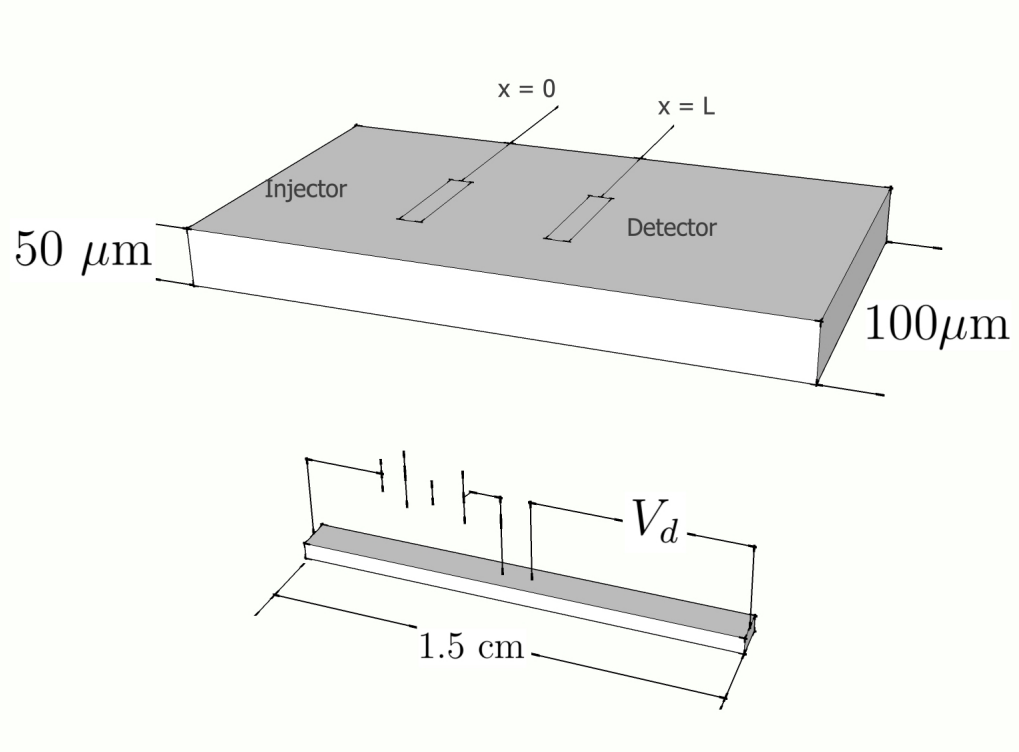

Figure 1.4 Schematic diagram of Johnson and Silsbee's first non-local spin injection and detection experiment [53].

.

TMR or MRAM, in which it is the spin polarized currents that carry both charges and spins [31, 24]. In NLSV spin and charge currents can be separated. In metal based NLSV, when spin polarized charge current is injected from FM into NM, non-equilibrium spin population is accumulated at the vicinity of FM/NM interface or FM/I/NM tunnel junction. Then the accumulated spin can diffuse to both directions in NM. In the direction where there is no charge flow, pure spin current forms. Such an idea of spin injection was first proposed theoretically in 1976 to generate non-equilibrium spin population in NM [18]. In experiment, Johnson and Silsbee first realized the non-local spin injection in 1985 in the micro scale sample which composed of Aluminum bar and two ferromagnetic bars [53]. The geometry of Johnson and Silsbee's experiment is shown in figure 1.4.

At Johnson's time, due to the lack of nanoscale fabrication technique, two FM electrodes distance is as large as 50 μm, therefore only a very small spin current signal of about 50 pV was detected. in 2001, the nano-scale Py/Cu/Py NLSV was fabricated by Jedema et al. with Py ($Ni_{80}Fe_{20}$) electrodes spacing of 250 nm as show in figure 1.5. Non-local spin signal was enhanced to 1.5 mΩ at 4.2 K and 0.4 mΩ at room temperature [49]. After Jedema et al.'s following work of Hanle spin precession in $Al/Al_2O_3/Co$ NLSV in 2002 [50], intensive study started to concentrate on NLSV as spintronic device because it is an effective tool to get spin diffusion length in different materials. Typical study on NLSV include metal based, semiconductor based and superconductor based devices.

For metal based NLSV, most work were concentrated on detection of spin diffusion length for different materials and ways to promote spin diffusion length such as the inclusion of MgO tunnel barrier. Otani's group also showed that large spin accumulation with spin diffusion length of 700 nm for Ag and 400 nm for Cu in Py/Ag/Py and Py/Cu/Py NLSV [37, 57]. In addition, Otani's group also found the non-local spin signal in Py/MgO/Ag NLSV can be enhanced 100 fold, up to 100 mΩ at 10 K, with MgO serves as tunnel barrier [33].

However, unlike Al, Ag, Cu and Mg, some heavy metal such as Pt, which has strong spin-orbit coupling, does not show spin transport over a long distance. In order to quantitatively analyze the spin transport property, spin relaxation time and the corresponding spin diffusion length are measured in NLSV with parallel magnetic field and perpendicular magnetic field [46]. By fitting the exponential decay of non-local spin signal with two FMs distances with parallel magnetic field applied, or by fitting the spin precession Hanle effect, one can extract the longitudinal spin diffusion length and transverse spin diffusion length [33].

Once non-equilibrium spin population is generated from direct spin injection in the NLSV, pin relaxation in NM is the process that spin equilibrium is reached. In

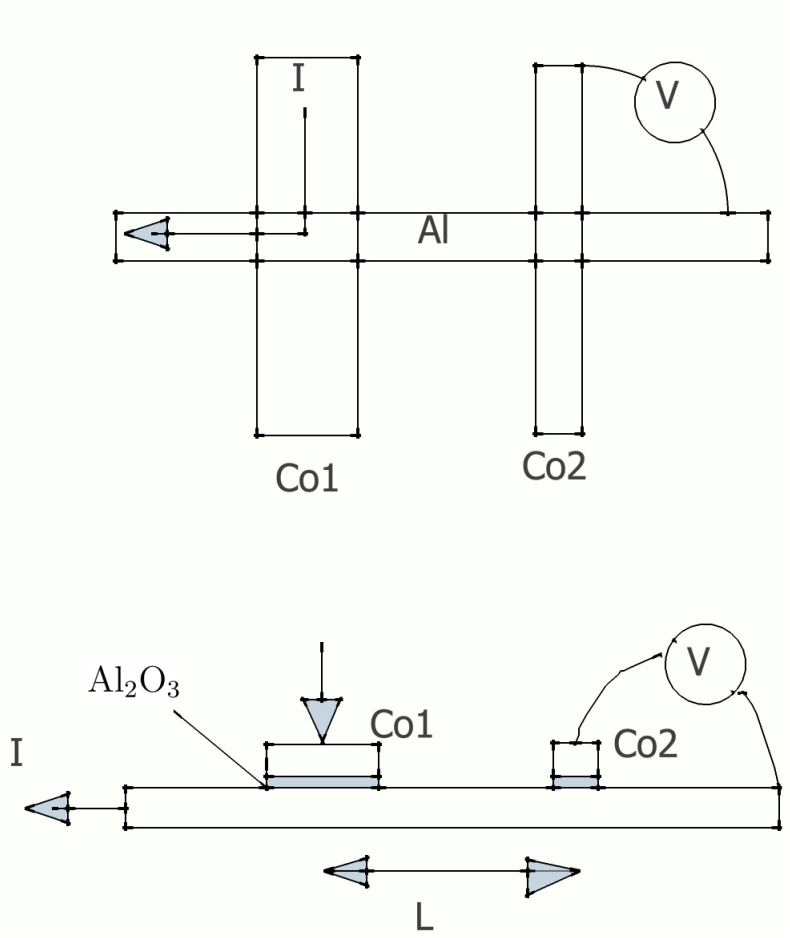

Figure 1.5 Schematic diagram of Jedema et al.'s nano-scale $Al/Al_2O_3/Co$ NLSV [50].

.

normal metal, the spin relaxation time is often of the order of nanosecond which is relatively long to use spin as information carrier. In isotropic metals, the longitudinal spin relaxation time often equals to transverse spin relaxation time [33, 96].

It is generally believed that Elliott-Yafet mechanism is suitable for most simple metals [96]. Elliott first proposed theory of conduction electron spin relaxation [30]. In his theory, spins relax through ordinary momentum scattering (impurities at low temperature or phonos at high temperature) with spin-orbit coupling induced by

lattice ions. The spin-orbit interaction is expressed as

$$V_{SO} = \frac{\hbar}{4m^2c^2}\nabla V_{SC} \times \hat{\vec{p}} \cdot \hat{\vec{\sigma}}, \tag{1.2}$$

where m is the electron mass, V_{SC} the spin dependent scalar potential, $\hat{\vec{p}} \equiv -i\hbar\nabla$ the linear momentum operator, $\hat{\vec{\sigma}}$ the Pauli matrices. By considering time-reversal symmetry and space reversal symmetry, Elliot got the two Bloch states for spin up $|\uparrow\rangle$ and spin down $|\downarrow\rangle$ electrons with band index n and lattice momentum $\vec{k}$,

$$\Psi_{\vec{k}n\uparrow}(\vec{r}) = [a_{\vec{k}n}(\vec{r})\,|\uparrow\rangle + b_{\vec{k}n}(\vec{r})\,|\downarrow\rangle]e^{i\vec{k}\cdot\vec{r}}, \tag{1.3}$$

$$\Psi_{\vec{k}n\downarrow}(\vec{r}) = [a^{\star}_{-\vec{k}n}(\vec{r})\,|\downarrow\rangle - b^{\star}_{-\vec{k}n}(\vec{r})\,|\uparrow\rangle]e^{i\vec{k}\cdot\vec{r}}, \tag{1.4}$$

where a and b are the complex lattice-periodic coeffecients, $\vec{r}$ the radius vector. Considering the fact that $|a|$ is close to 1, while $|b| \ll 1$ in most cases, we can also call $\Psi_{\vec{k}n\uparrow}$ and $\Psi_{\vec{k}n\downarrow}$ spin up and spin down states.

To understand the spin relaxation process, perturbation method is used. Considering a band structure without spin-orbit coupling, the addition of V_{SO}, which is periodic in the lattice, couples electrons with opposite spins which have the identical $\vec{k}$ while different n. The distance between bands is normally a lot larger than spin-orbit coupling, which is treated as a small perturbation. Therefore, we have

$$|b| \approx \lambda_{SO}/\Delta E \ll 1, \tag{1.5}$$

where ΔE is the nearest bands distance for quantum states in the bands, λ_{SO} the matrix element amplitude of V_{SO}. Thus, Elliott got the conclusion that spin-orbit coupling, in combination with momentum scattering, mixes the spin-up and spin-down states and results in spin relaxation. At low temperature, momentum scattering is originated from scattering of impurity such as boundaries and defects. At high temperature T, momentum scattering is mainly caused by phonons. The spin-orbit interaction, which is modified by phonons, can directly couple spin down and spin up states [93].

Spin-orbit coupling is generally believed to be proportional the the forth power of atomic number [78].

That's why in experiment, the spin relaxation time in heavy metals, such as Au, Pt, is shorter than light metals. However, as we see in eq. 1.5 the electronic structure also influence spin relaxation [46].

Another origin of spin relaxation in NLSV was found to be from surface spin scattering of nanowires. Idzuchi et al. found an MgO capping layer on Ag nanowires can effectively suppress surface scattering induced spin flip events in Py/Ag non-local lateral spin valve. With all the origins of spin relaxation included, the spin relaxation time could be expressed as [45]

$$\frac{1}{\tau_{sf}} = \frac{1}{\tau_{sf}^{ph}} + \frac{1}{\tau_{sf}^{imp}} + \frac{1}{\tau_{sf}^{surf}}, \tag{1.6}$$

where τ_{sf}^{ph}, τ_{sf}^{imp} and τ_{sf}^{surf} are the phonon, impurity and surface induced spin relaxation time. The possible explanation of surface spin relaxation is dominated spin-orbit interaction [65, 1]. The surface spin flip scattering probability is of the order of magnitude of $e^2Z/\hbar c$, where Z is the atomic number. The MgO capping layer reduces the formation of AgO_x layer on the surface of the nanowire, therefore reduces the effective Z by introducing Mg which has much smaller Z than Ag. Thus the surface scattering is reduced [45].

1.3 Drift-diffusion Model for Non-local Spin Valve

The drift-diffusion model of spin transport in disordered systems is a classical model based on Drude's theory of electrical conduction. Drude's theory used the kinetic theory of gases on a metal by assuming a gas of electrons in the metal. Although more serious theory of conduction electrons should be based on quantum theory, Drude's model is still of immense value. Drude's theory is based on several fundamental assumptions: 1, the independent electron approximation and free electron approxi-

mation; 2, collisions are instantaneous events that abruptly change electron velocity by assuming there is some scattering mechanism no matter what it might be; 3, an electron experiences a collision with a probability per unit time $1/\tau$; 4, electrons can achieve thermal equilibrium with the environment only by collisions [8].

Consider an electron undergoing random walk in a one dimensional disordered system, the electron mean free path is l. The electron move with velocity of v before change direction by scattering. The time of flight is $\tau = l/v$. With the applied electric field E, which is small enough ($\Delta v = eE\tau/m \ll v$) not to significantly alter v, a biased random walk forms. Therefore the average velocity of the electron is given by

$$\dot{v}_{av} = -\frac{eE}{m} - \frac{v_{av}}{\tau}. \tag{1.7}$$

In steady state, the average velocity is defined as drift velocity v_d by letting $\dot{v}_{av} = 0$,

$$v_d = -\frac{v\tau_{av}}{\tau}. \tag{1.8}$$

Typically in metal, v_d is of the order of 1 cm/s while $v \approx 10^6$ m/s. The electron flow correspondingly leads to change of density $n(x,t)$ at position x and time t. Where $n(x,t)$ satisfies the normalization condition at all times as

$$N_0 = \int_{-\infty}^{\infty} n(x,t)\mathrm{d}x, \tag{1.9}$$

where it is reasonably assumed that N_0 electrons can not be either created or destroyed.

By analyzing the diffusive random walk, the drift velocity and change of density is related by the drift-diffusion differential equation

$$\frac{\partial n}{\partial t} = D\frac{\partial^2 n}{\partial x^2} - v_d\frac{\partial n}{\partial x}, \tag{1.10}$$

where $D = l^2/2\tau = v^2\tau/2$ is diffusion coefficient. Usually for the metal at room temperature, τ is of the order of 10^{-14} s. D is of the order of 10^{-2} $\mathrm{m^2 s^{-1}}$.

Suppose a delta-like initial distribution of $n(x,0) = N_0\delta(x)$, at a later time t, the center moves at drift velocity v_d under the influence of electric field:

$$v_d = -\frac{e\tau}{m}E, \tag{1.11}$$

where $\mu = e\tau/m$ is defined as electron mobility. In metal, the mobility is often of the order of 10^{-3} m^2/Vs.

While due to diffusion, the probability distribution broadens proportional to $\sqrt{t}$ as

$$n(x,t) = \frac{N_0}{\sqrt{4\pi Dt}}e^{-x^2/4Dt}. \tag{1.12}$$

The drift-diffusion equation can now be rewritten as

$$\frac{\partial n}{\partial t} + \frac{\partial}{\partial x}[-\mu nE - D\frac{\partial n}{\partial x}] = 0, \tag{1.13}$$

in which we can introduce electron current as

$$J = -\mu nE - D\frac{\partial n}{\partial x}, \tag{1.14}$$

where the first term describes the drift current and the second term the diffusion current. The corresponding electrical current is given as

$$j = -eJ = \sigma E + eD\frac{\partial n}{\partial x}, \tag{1.15}$$

in which $\sigma = e\mu n$ is the conductivity. The corresponding resistivity is $\rho = 1/\sigma$.

With the definition of the electron (particle) current J, eq. 1.13 can be expressed as

$$\frac{\partial n}{\partial t} + \frac{\partial J}{\partial x} = 0, \tag{1.16}$$

which is just the continuity equation describing the conservation of particles.

When electron spin is put into consideration, the total electron density n and the electron density for spin up and spin down, $n_\uparrow$ and $n_\downarrow$, satisfy

$$n = n_\uparrow + n_\downarrow, \tag{1.17}$$

the spin density is given by

$$s = n_\uparrow - n_\downarrow. \tag{1.18}$$

Different from particle drift-diffusion, there is the possibility w for spins to be flipped in the time τ. So we can get the spin flip rate w/τ. The typical spin flip probability after relaxation time τ is 10^{-6} to 10^{-3}, which means an electron gets its spin flipped after thousands of scatterings. Similar to eq. 1.10, the drift-diffusion equations for $n_\uparrow$ and $n_\downarrow$ is

$$\frac{\partial n_\uparrow}{\partial t} = D\frac{\partial^2 n_\uparrow}{\partial x^2} - v_d\frac{\partial n_\uparrow}{\partial x} - w(n_\uparrow - n_\downarrow), \tag{1.19}$$

$$\frac{\partial n_\downarrow}{\partial t} = D\frac{\partial^2 n_\downarrow}{\partial x^2} - v_d\frac{\partial n_\downarrow}{\partial x} - w(n_\downarrow - n_\uparrow). \tag{1.20}$$

Adding the above equations recovers eq. 1.10. However, subtracting eq. 1.20 from eq. 1.19 yields drift-diffusion equation for s:

$$\frac{\partial s}{\partial t} = D\frac{\partial^2 s}{\partial x^2} - v_d\frac{\partial s}{\partial x} - \frac{s}{\tau_s}, \tag{1.21}$$

where $1/\tau_s = 2w/\tau$ gives the spin relaxation. τ_s is spin relaxation time. By substituting the drift velocity with mobility, we can rewrite the spin version of continuity equation

$$\frac{\partial s}{\partial t} + \frac{\partial}{\partial x}(-\mu E s - D\frac{\partial s}{\partial x}) = -\frac{s}{\tau_s}, \tag{1.22}$$

from which we get the spin particle current

$$J_s = -\mu E s - D\frac{\partial s}{\partial x}. \tag{1.23}$$

The spin (charge) current can be written as

$$j_s = -eJ_s = \sigma_s E + eD\frac{\partial s}{\partial x}, \tag{1.24}$$

where $\sigma_s = e\mu s$ is the spin conductivity.

For the case of $E = 0$, the electric field which induce spin drift is neglected. Eq. 1.22 can be solved for different boundary and initial conditions. For a delta function

like initial spin density, which means at $t = 0$, $s(x, 0) = S_0\delta(x)$, we can solve spin diffusion equation

$$\frac{\partial s}{\partial t} = D\frac{\partial^2 s}{\partial x^2} - \frac{s}{\tau_s}. \tag{1.25}$$

The solution is

$$s(x, t) = \frac{S_0}{\sqrt{4\pi Dt}} e^{-x^2/4Dt} e^{-t/\tau_s}, \tag{1.26}$$

in which the two exponential terms give spin diffusion and spin relaxation. The spatial spin distribution deviation at time $t = \tau_s$ gives the spin diffusion length

$$l_s = \sqrt{D\tau_s} = \sigma/\sqrt{2}. \tag{1.27}$$

For the case of steady state, i. e. $\partial s/\partial$ t=0, we have

$$D\frac{\partial^2 s}{\partial x^2} = \frac{s}{\tau_s}, \tag{1.28}$$

with spin source at $x = 0$, $s(0) = s_0$, $s(\infty) = 0$, the solution to eq. 1.28 is

$$s(x) = s_0 e^{-x/\sqrt{D\tau_s}} = s_0 e^{-x/l_s}, \tag{1.29}$$

which means the spin can spread l_s from the spin source at $x = 0$.

For case of steady spin current at $x = 0$, i. e. $J_s(0) = -D\partial s/\partial x|_{x=0} = J_{s0}$, the solution of eq. 1.28 is

$$s(x) = J_{s0}\frac{l_s}{D} e^{-x/l_s}. \tag{1.30}$$

At $x = 0$, the spin is

$$s(0) = J_{s0}\frac{l_s}{D}. \tag{1.31}$$

1.4 Spin dynamics: Hanle effect

The drift-diffusion model can also be generalized for spin dynamics. With the existence of external magnetic field, the spin will precess as

$$\frac{\mathrm{d}\mathbf{s}}{\mathrm{d}t} = \mathbf{s} \times \boldsymbol{\omega}_L, \tag{1.32}$$

where $\boldsymbol{\omega}_L = \gamma \mathbf{B}$ is directed Larmor frequency, $\gamma = 2\mu_{\mathrm{B}}/\hbar$ the gyromagnetic ratio, μ_{B} the Bohr magneton. with random walk put into consideration, the spin dynamics drift-diffusion equation is

$$\frac{\partial \mathbf{s}}{\partial t} = \mathbf{s} \times \boldsymbol{\omega}_L + D\nabla^2 \mathbf{s} + \mu E \nabla \mathbf{s} - \frac{\mathbf{s}}{\tau_s}. \tag{1.33}$$

The continuity equation with spin dynamics is

$$\frac{\partial \mathbf{s}}{\partial t} - \nabla[\mu E \mathbf{s} - D\nabla \mathbf{s}] = \mathbf{s} \times \boldsymbol{\omega}_L - \frac{\mathbf{s}}{\tau_0}, \tag{1.34}$$

in which we have the generalized spin current

$$\mathbf{J}_s = -\mu E \mathbf{s} - D\nabla \mathbf{s}. \tag{1.35}$$

Then the spin charge current becomes

$$\mathbf{j}_s = -e\mathbf{J}_s = e\mu E \mathbf{s} + eD\nabla \mathbf{s}. \tag{1.36}$$

Correspondingly the continuity equation becomes

$$\frac{\partial \mathbf{s}}{\partial t} + \nabla \mathbf{J}_s = \mathbf{s} \times \boldsymbol{\omega}_L - \frac{\mathbf{s}}{\tau_s}. \tag{1.37}$$

The Hanle effect describes the spin precession in NM with magnetic field applied perpendicular to the initially injected spin from injector FM in the structure of NLSV. The detector at some distance from the injector detects the average spin. Due to the spin precession, coherent spin precession angle could be identified with increasing perpendicular magnetic field. While due to the diffusive transport, a continuous decrease of spin accumulation could also be identified. From injector to detector, different electrons experience different transit time, the corresponding precession angles are also different.

The analytical expression of Hanle effect can be derived for diffusive pure spin current based from transit-time distribution model. For a single spin, the probability

on time t for the spin to transit a distance L from injector to detector with random walk is

$$P(t) = \frac{1}{\sqrt{4\pi Dt}} e^{-L^2/4Dt}. \tag{1.38}$$

Statistically for all the spins, $P(t)$ is proportional to the number of electrons, injected at $x = 0$ from injector, arriving at the detector at $x = L$ after diffusion time t. The spin relaxation contributes another exponential term $\exp(-t/\tau_s)$ to the number of spins arriving at $x = L$. With the Larmor precession which contributes the term $\cos(\omega_L t)$, the statistical average of all the spins' contribution to the non-local spin valve signal equals to the time integral of $P(t)\exp(-\tau_s/t)\cos(\omega_L t)$,

$$V(B_\perp)/I \propto \int_0^\infty P(t)\cos(\omega_L t)\mathrm{e}^{-t/\tau_s} dt. \tag{1.39}$$

The coefficient could be determined by comparing non-local spin signal at no spin precession, i. e. $B_\perp = 0$, with the spin signal from parallel magnetic field applied [50, 96] as

$$V(B_\perp)/I = \frac{1}{e^2 N(\varepsilon_F) A} \int_0^\infty P(t)\cos(\omega_L t)\mathrm{e}^{-t/\tau_s} dt, \tag{1.40}$$

where $N(\varepsilon_F)$ is density of states at Fermi energy.

Therefore, perpendicular magnetic field can control coherent spin precession in NLSV. Some key parameters such as spin diffusion length, spin polarization and the transit time for $\pi/2$ and π precession can be derived from fitting the measured spin Hanle curve [96, 50].

1.5 Motivation and Thesis Outline

For the past decade, most work related to NLSV concentrate on the detection of spin diffusion length of different materials in normal metal, semiconductor and superconductor [96, 36, 50, 84, 33, 38, 64, 26, 39]. In this work, for the first time, we designed and fabricated a FM(Co, Py)/MgO/Al NLSV with a ring spacer. In such a geometry, we observe the Aharonov-Bohm interference effect and Hanle effect

together with precessing spin current or spin polarized electric current for the first time. By comparing the spin precession period and spin transit time in the ring from Hanle effect, the adiabaticity of quantum transport can be analyzed. Therefore, the our observation can also be understood as the observation of Aharonov-Anandan non-adiabatic geometric phase.

In addition, Aluminum is superconductor below T_C, our designed NLSV interferometer also a tool for the research of spin transport in superconductor. It is also interesting to observe the interference effect in superconducting state aluminum ring with non-local spin injection.

The NLSV is designed such that, in the injection region, it is an S/F/S lateral Josephson junction to generate long range triplet components in the FM bar. It is interesting to see whether such a triplet correlation can spread out into superconductor and be detected in non-local manner, i. e. the direct observation of superconducting spin current. It is also very interesting to observe the interference effect with superconducting spin current.

In Chapter 2, I will review the Aharonov-Bohm phase, Berry's adiabatic geometric phase and Aharonov-Anandan's non-adiabatic geometric phase. Their relationship will also be discussed. Some experimental observation of either adiabatic or non-adiabatic geometric phase will also be reviewed.

In Chapter 3, I will review the theories about phase coherent transport in the disordered mesoscopic conductor. Weak localization and AAS oscillation will also be discussed as they appeared in our measured result.

In Chapter 4, I will discuss the sample fabrication of NLSV interferometer and measurement.

In Chapter 5, the measured result on the NLSV interferometer will be discussed. Injector-detector Distance dependence of spin resistance and Hanle effect measurement are fitted to the theoretical model. Spin diffusion length is distracted from the

curve fitting. h/e oscillation was found on the non-local Hanle effect curve. For the local magnetoresistance measurement with spin polarized current, both h/e and $h/2e$ were found.

In Chapter 6, the measurement of spin resistance in superconducting state Aluminum in the NLSV interferometer is analyzed. Spin resistance is identical in normal and superconducting states, which disagrees with theoretical prediction based on quasiparticle picture. Considering in the injector region it is an S/F/S Josephson junction which can generate triplet supercurrent in FM bar, we suggested that, the triplet correlation in FM can also spread out into the type I superconductor like Al.

Chapter 2

Geometric Phase

In this chapter, I will review the Aharonov-Bohm phase, Berry phase and Aharonov-Anandan non-adiabatic geometric phase.

2.1 Aharonov-Bohm Phase

In classical mechanics, the motion of a particle is driven by a force on it, which obeys Newton's second law. Such forces, if we try to find out the origin, come from gravitational field or electro-magnetic field. The electric and magnetic fields are described in the from of Maxwell equations in the vacuum as

$$\boldsymbol{\nabla} \cdot \mathbf{E} = \frac{\rho}{\epsilon} \tag{2.1}$$

$$\boldsymbol{\nabla} \cdot \mathbf{B} = 0 \tag{2.2}$$

$$\boldsymbol{\nabla} \times \mathbf{E} = -\frac{\partial \mathbf{B}}{\partial t} \tag{2.3}$$

$$\boldsymbol{\nabla} \times \mathbf{B} = \mu_0 \mathbf{J} + \mu_0 \epsilon_0 \frac{\partial \mathbf{E}}{\partial t} \tag{2.4}$$

For a charged particle, the force applied on it is Lorentz force

$$\mathbf{F} = e(\mathbf{E} + \mathbf{v} \times \mathbf{B}). \tag{2.5}$$

In classical electromagnetic theory, together with boundary conditions, the above equations can explain electromagnetic phenomena. Two more fundamental quantities which are directly related to the charges and current sources of ρ_0 and $\mathbf{J}_0$ are scalar

potential ϕ and vector potential $\mathbf{A}$. Once ϕ and $\mathbf{A}$ are determined from sources, $\mathbf{E}$ and $\mathbf{B}$ fields can be easily derived as

$$\mathbf{B} = \boldsymbol{\nabla} \times \mathbf{A} \tag{2.6}$$

$$\mathbf{E} = -\boldsymbol{\nabla}\phi - \frac{\partial \mathbf{A}}{\partial t}. \tag{2.7}$$

At early time, it is generally believed that scalar potential and vector potential are useful mathematical tools which simplify the description of electromagnetic fields from six components to four components. It is initially considered they have no physical significance.

In 1959, Yakir Aharonov and David Bohm proposed a thought experiment and predicted that, for a charged particle, in the region where there is no field which acts any forces on this particle, the vector potential still affects this charged particle, in the form of its quantum phase. As shown in figure 2.1, a magnetic flux of

$$\Phi_B = \pi r^2 \hat{\mathbf{z}} \cdot \mathbf{B} = \pi r^2 B_z = 2\pi r \hat{\boldsymbol{\phi}} \cdot \mathbf{A} \tag{2.8}$$

exists in the center of the ring but not on the ring itselt. An electron beam split into two beams at the left of the ring. Two beams pass through two arms of the ring where no magnetic field $\mathbf{B}$ exists but only vector potential $\mathbf{A}$ exists. So there's no actual electromagnetic force originated from the flux Φ_B acting on the two electron beams. The quantum wave function phase difference from up and bottom arms is

$$\left[\left(\frac{e}{\hbar}\right)\int_{\mathbf{x}_1}^{\mathbf{x}_N} \mathbf{A}\cdot \mathrm{d}\mathbf{s}\right]_{top} - \left[\left(\frac{e}{\hbar}\right)\int_{\mathbf{x}_1}^{\mathbf{x}_N} \mathbf{A}\cdot \mathrm{d}\mathbf{s}\right]_{bottom} = \left(\frac{e}{\hbar}\right)\oint \mathbf{A}\cdot \mathrm{d}\mathbf{s} = \left(\frac{e}{\hbar}\right)\Phi_B. \tag{2.9}$$

Such a phase difference could be detected by the interference effect of two electron beams by changing the magnetic field B_z and the corresponding magnetic flux Φ in the ring. In other words, while changing B_z, the probability of observing the particle at the right of the ring will show a sinusoidal change as

$$\left(\frac{e}{\hbar}\right)\Phi_B = 2\pi\frac{e}{h}\Phi_B = 2\pi\left(\frac{\Phi_B}{\Phi_0}\right) = 2\pi\left(\frac{\pi r^2 B_z}{\Phi_0}\right), \tag{2.10}$$

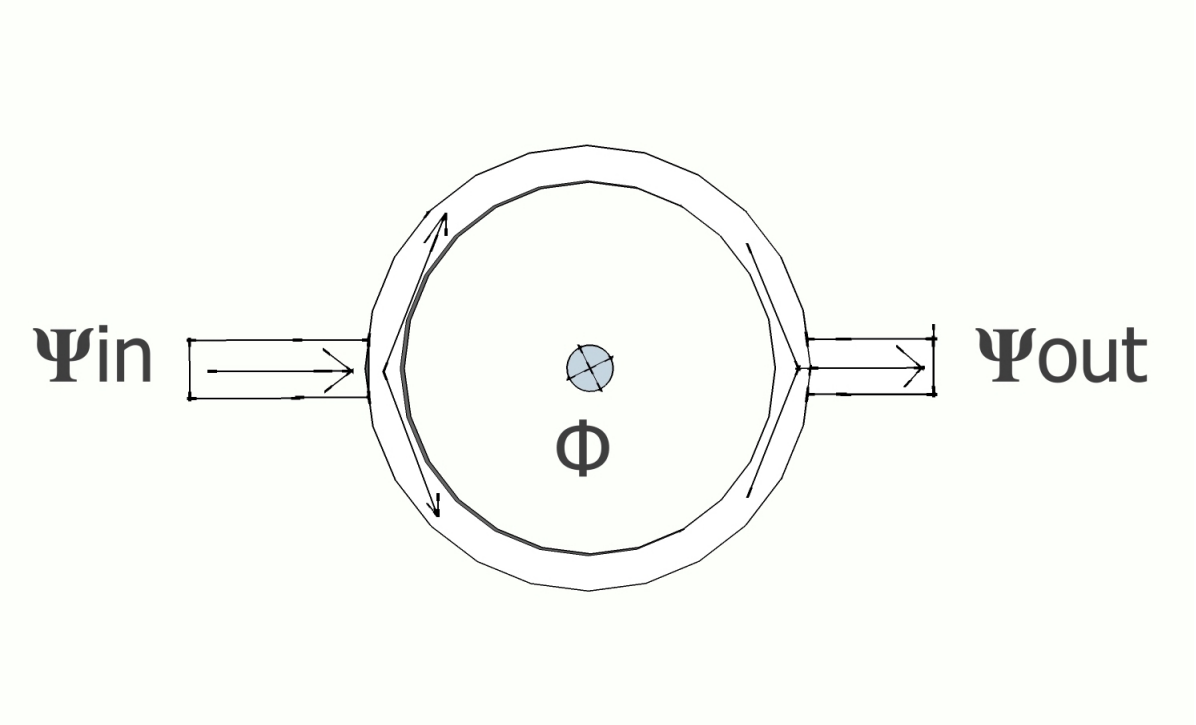

Figure 2.1 Schematic diagram of interference effect proposed by Y. Aharonov and D. Bohm. The radius of the ring is r.

where $\Phi_0 = h/e$.

Since Y. Aharonov and D. Bohm proposed the AB effect, the h/e interference have been experimentally observed in different physical systems. Early experiment was performed in vacuum in a modified scanning electron microscope where the electron beam is generated and detected. The apparatus of electrostatic biprism was introduced to separate an electron beam into two, such that the magnetic flux, originated from an 1 μm diameter and 0.5 mm long iron whisker, could be applied between two beams as shown in figure 2.2 [22].

Due to the high voltage applied in the electron microscope to accelerate the electrons to form electron beams, the De Broglie wavelength of the electron is to order of 1 nm, which is much smaller than the typical size of apparatus which is to the order of several micrometer. By examining the interference pattern, The AB effect

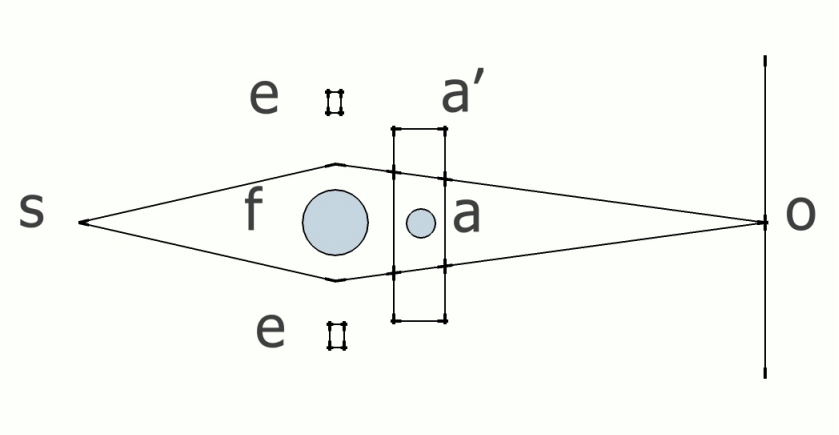

Figure 2.2 Schematic diagram of biprism type Aharonov-Bohm interferometer from [22]. s is electron source, o is observing plane, e and f is biprism, a and a' are confined and extended field regions.

was observed. A similar experiment with more complex apparatus was performed later with consistent result [86].

The early experiments were performed in the vacuum such that the electron wave function can maintain its phase coherence naturally without any scattering. However in the metal, it was initially thought that AB effect could not be observed because of scattering in the electron transport. Until in the 1980s, with the development of low temperature technique and electron beam lighthography, the electrical measurement of sub-micro sized sample at extremely low temperature of milliKelvin level could be realized. The AB effect was observed in Au metal ring with diameter smaller than 1 μm at 10 mK [91]. The magnetoresistance oscillation with period corresponding to flux h/e was clearly observed in a 784 nm diameter ring as shown in figure 2.3 from [91].

The importance of this work is it not only confirmed the AB effect, but also showed that, even though electrons experience a lot of elastic scattering from defects, boundaries and impurities while diffusively transporting in disordered Au metal wire at very low temperature at which the inelastic scattering from phonons is substantially

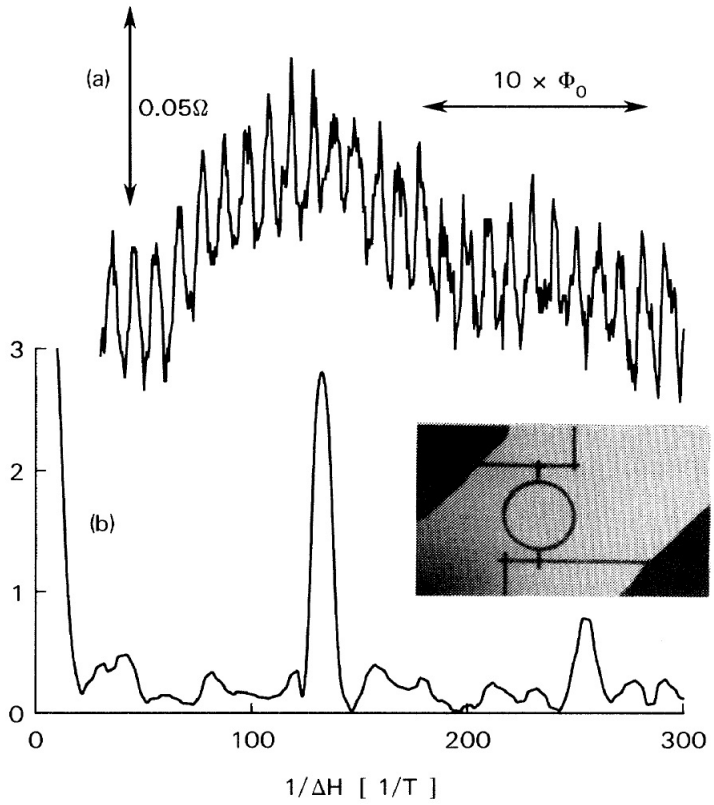

Figure 2.3 Magnetoresistance oscillation and corresponding Fourier transform observed in Au ring from [91].

suppressed, electrons can still maintain their phase coherence for a length scale defined as phase coherence length L_ϕ, which is longer than the electron mean free path L_f. Later it was proved that inelastic scattering such as electron phonon scattering, electron-electron scattering can break the phase coherence [91, 23, 27, 90]. Together with theoretical and experimental work on weak localization, AB effect experiment in ring structures serve as the foundation of modern mesoscopic physics. The details will be discussed in Chapter 3.

2.2 Adiabatic Geometric Phase: Berry Phase

Aharonov-Bohm effect was later theoretically reformulated by Berry as a special case of adiabatic geometric phase which was later generally called Berry Phase [16]. M.

V. Berry showed that for a quantum system which is in its energy eigenstate, slowly evolved around a closed circuit in the parameter space, will acquire a geometric phase $\exp(i\gamma)$ except the familiar dynamical phase, when the quantum system comes back to its original quantum state. Berry derived the geometric phase as follows. Suppose the Hamiltonian H can be changed by the external parameters $\mathbf{R} = (X, Y, ...)$. Let the quantum system to transport around a closed circuit C in the parameter space $\mathbf{R}(t)$ from $t = 0$ to $t = T$ such that the Hamiltonian $H(\mathbf{R}(t))$ changes accordingly. The quantum state $|\psi(t)\rangle$ evolves with time as described by Schrodinger equation

$$H(\mathbf{R}(t))\,|\psi(t)\rangle = i\hbar\,|\dot{\psi}(t)\rangle\,. \tag{2.11}$$

The instantaneous orthonormal basis can be chosen as the energy eigenstates of $H(\mathbf{R})$ for $\mathbf{R} = \mathbf{R}(t)$, which is expressed as

$$H(\mathbf{R})\,|n(\mathbf{R})\rangle = E_n(\mathbf{R})\,|n(\mathbf{R})\rangle\,, \tag{2.12}$$

with corresponding energies $E_n(\mathbf{R})$.

According to adiabatic theorem in quantum mechanics, as stated by Max Born and Vladimir Fock, a quantum system which is initially at one of its eigenstates $|n(\mathbf{R}(0))\rangle$ will remain as the instantaneous eigenstate of the Hamiltonian $H(\mathbf{R}(t))$ at a later time t [20].

Therefore, $|\psi(t)\rangle$ at a later time t can be expressed as

$$|\psi(t)\rangle = \exp\Big\{-\frac{i}{\hbar}\int_0^t \mathrm{d}r' E_n(\mathrm{R}(t'))\Big\}\exp(i\gamma_n(t))\,|n(\mathbf{R}(t))\rangle\,, \tag{2.13}$$

in which the first exponential term is the dynamical phase.

Another phase factor $\gamma_n(t)$ can be determined by putting $\psi(t)$ into Schrodinger equation. This leads to

$$\dot{\gamma}_n(t) = i\,\langle n(\mathbf{R}(t))|\boldsymbol{\nabla}_{\mathbf{R}} n(\mathbf{R}(t))\rangle\cdot\dot{\mathbf{R}}(t). \tag{2.14}$$

At time T the quantum state is given by

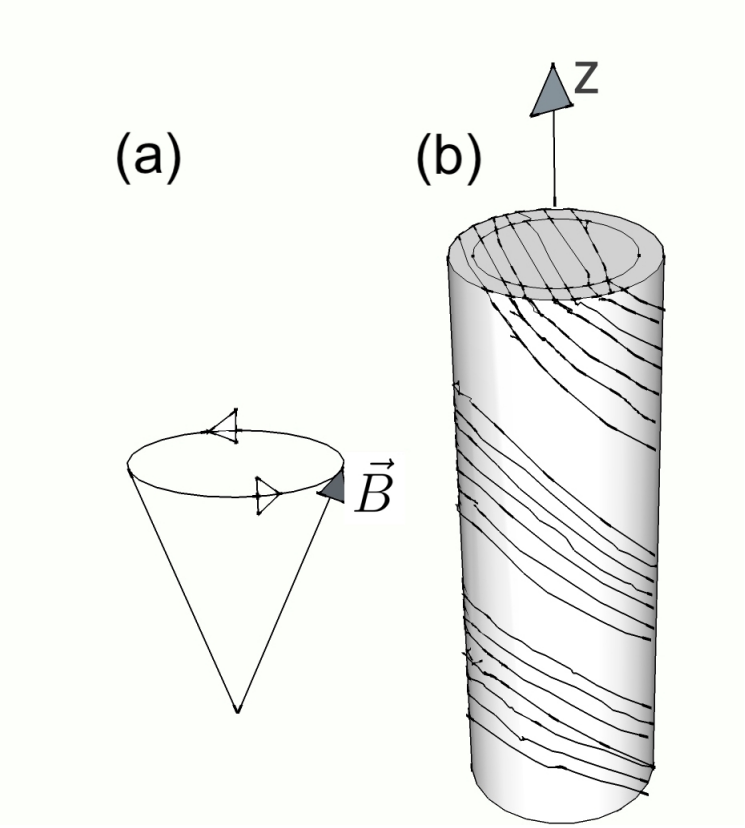

Figure 2.4 Berry's first thought experiment was experimentally observed with polarized neutron beam that pass through a long cylinder with helical coil on it. (a) The helical coil generated varying magnetic field which finally goes back to the original direction. (b) The cylinder with helical coil from [19].

$$|\psi(T)\rangle = \exp(i\gamma_n(C))\exp\left\{-\frac{i}{\hbar}\int_0^T \mathrm{d}t E_n(\mathbf{R}(t))\right\}|\psi(0)\rangle\,, \tag{2.15}$$

where the geometric phase factor is

$$\gamma_n(C) = i\oint_C \langle n(\mathbf{R}|\boldsymbol{\nabla}_{\mathbf{R}} n(\mathbf{R})\rangle \cdot \mathrm{d}\mathbf{R} \tag{2.16}$$

From eq. 2.16, it is found that the closed circuit integral in parameter space alone give the phase factor $\gamma_n(C)$, which is independent of how $\mathbf{R}(t)$ varies in time. That is why the phase factor is named as geometric phase.

One example Berry discussed in his original paper is a spin which is always parallel with external magnetic field, whose direction changes adiabatically and finally returns

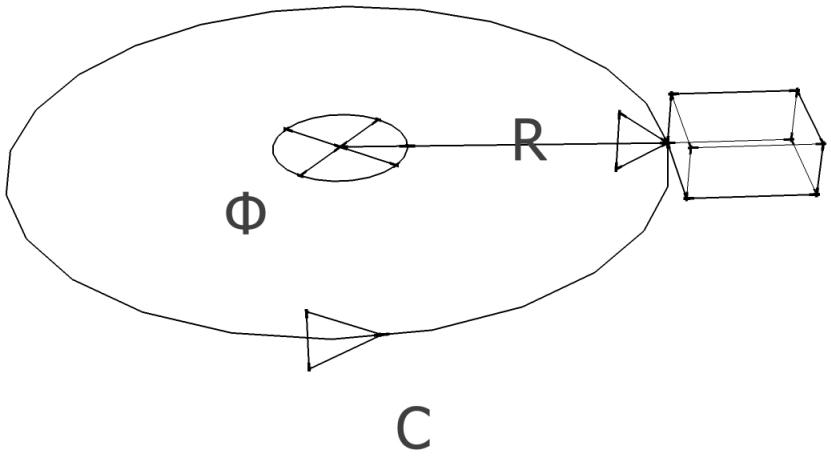

Figure 2.5 In the center of the ring, suppose a flux line generate Φ. The radius of the ring is R. An electron is confined in a box which moves slowly around the trajectory C and goes back to original position.

back to the original direction. The spin finally accumulates a geometric phase factor relates to the solid angle that **B** subtends during the adiabatic change of direction. This thought experiment was shortly realized in 1987 by Bitter et. al who used spin polarized neutron beam that passes along the center of a long cylinder inside which the helical coil generated slowly varying **B** field as shown in figure 2.4 [19].

Berry also found that the Aharonov-Bohm effect could be viewed as a consequence of geometric phase. As shown in figure 2.5, suppose a box which can confine an electron move along a closed ring C. a flux line Φ is located in the center of the ring. Vector **R** connects the origin point and a reference point in the box. Therefore the external parameter is **R** itself in real space. Vector potential is related with magnetic

field and flux as $2\pi\hat{\boldsymbol{\phi}} \cdot \mathbf{A} = \pi R^2 \mathbf{B} \cdot \hat{\mathbf{z}} = \Phi$. In this case, the Hamiltonian is a function of position $\hat{\mathbf{r}}$ and momentum as

$$H = H(\mathbf{p}, \mathbf{r} - \mathbf{R}). \tag{2.17}$$

The eigenvalue E_n is independent of $\mathbf{R}$. The corresponding wavefunctions are $\psi_n(\mathbf{r} - \mathbf{R})$. Considering the flux line, eigenvalue equation is

$$H(\hat{\mathbf{p}} - q\mathbf{A}(\hat{\mathbf{r}}), \hat{\mathbf{r}} - \mathbf{R}) \left| n(\mathbf{R}) \right\rangle = E_n \left| n(\mathbf{R}) \right\rangle . \tag{2.18}$$

The nth wave function can be expressed as

$$\langle \mathbf{r} | n(\mathbf{R}) \rangle = \exp\left\{ \frac{iq}{\hbar} \int_{\mathbf{R}}^{\mathbf{r}} \mathrm{d}\mathbf{r}' \cdot \mathbf{A}(\mathbf{r}') \right\} \psi_n(\mathbf{r} - \mathbf{R}) \tag{2.19}$$

Because in free space, electron can not transport in a curved trajectory. In this case, when the box transports around the closed circuit C, it is the confinement from the box that make the electron transport along the curve. The reflection from the box wall alters the direction of the electron transportation. Compared with the electron wavelength, the length scale between every two scattering from the box wall is a lot larger. The direction change is also gradual, therefore the adiabatic requirement is also satisfied. By applying eq. 2.16,

$$\begin{aligned} \langle n(\mathbf{R}) | \boldsymbol{\nabla}_{\mathbf{R}} \boldsymbol{n}(\mathbf{R}) \rangle &= \int\int\int \mathrm{d}^3\mathbf{r} \psi_n^*(\mathbf{r} - \mathbf{R}) \Big\{ -\frac{iq}{\hbar} A(\mathbf{R}) \psi_n(\mathbf{r} - \mathbf{R}) + \boldsymbol{\nabla}_{\mathbf{R}} \psi_n(\mathbf{r} - \mathbf{R}) \Big\} \\ &= -iq\mathbf{A}(\mathbf{R})/\hbar \end{aligned} \tag{2.20}$$

The gradient operator is with respect to $\mathbf{R}$, so it can be taken out of the space integral. From normalization condition of ψ_n, the phase factor can be calculated as

$$\gamma_n(C) = \frac{q}{\hbar} \oint_C \mathbf{A}(\mathbf{R}) \cdot \mathrm{d}\mathbf{R} = a\Phi/\hbar, \tag{2.21}$$

which is just the same as the AB phase.

2.3 Non-adiabatic Geometric Phase: Aharonov Anandan Phase

An important extension of Berry' geometric phase is the non-adiabatic generalization, which was proposed by Aharonov and Anandan in 1987 [2, 7]. In their paper the cyclic evolution of a quantum state without the restriction of adiabatic condition was analyzed. Such non-adiabatic generalization emphasizes the purely geometrical nature of phase which depends only on the geometry of pathway that the system evolves along. The adiabatic restriction was also removed by Berry who calculated the adiabatic correction terms [17].

After Aharonov and Anandan generalized geometric phase to the non-adiabatic cyclic evolution, the cyclic condition was removed by Samuel and Bhandary [76]. Garrison and Chiao generalized geometric phase to any classical complex multicomponent field, which means the pendants of quantal phase also exist in classical theories as Hannay angles [35, 40].

Aharonov-Anandan phase was derived by the introduction of the projective Hilbert space. First considering Schrodinger equation

$$H(t)\left|\psi(t)\right\rangle = i\hbar\frac{\mathrm{d}}{\mathrm{d}t}, \tag{2.22}$$

Suppose the period of cyclic evolution is T, the initial state $\psi(0) \in \mathcal{N}_0$ and final state $\psi(T) \in \mathcal{N}_0$ are related by

$$\left|\psi(T)\right\rangle = e^{i\Phi}\left|\psi(0)\right\rangle, \tag{2.23}$$

in which Ψ is real. $\mathcal{N}_0$ is the set of non-zero quantum states in $\mathcal{H}$, such that $\mathcal{N}_0 = \{|\psi\rangle \in \mathcal{H}|\, \langle\psi|\psi\rangle = 1\}$. The projective Hilbert space consists of all quantum states in $\mathcal{N}$ where the only difference is a phase factor. The projection map of

$$\Pi : \mathcal{N}_0 \to \mathcal{P} \tag{2.24}$$

is defined by

$$\Pi(|\psi\rangle) = \{|\psi'\rangle : |\psi'\rangle = c\,|\psi\rangle\}, \tag{2.25}$$

where c is a complex number. A curve C is defined by $|\psi\rangle$ as a closed curve in $\mathcal{P}$. $|\tilde{\psi}(t)\rangle$ is defined as

$$|\tilde{\psi}(t)\rangle = e^{-if(t)} |\psi(t)\rangle \tag{2.26}$$

with $f(t) - f(0) = \phi$. Then it is obvious

$$|\tilde{\psi}(\tau)\rangle = |\tilde{\psi}(0)\rangle \tag{2.27}$$

By applying Schrodinger equation,

$$-\frac{df}{dt} = \frac{1}{\hbar} \langle\psi(t)| H |\psi(t)\rangle - \langle\tilde{\psi}(t)| i\frac{d}{dt} |\tilde{\psi}(t)\rangle . \tag{2.28}$$

Then the dynamical part can be removed from ϕ by defining

$$\beta \equiv \phi + \hbar^{-1} \int_0^\tau \langle\psi(t)| H |\psi(t)\rangle \, dt. \tag{2.29}$$

By applying eq. 2.28, it gives

$$\beta = i \int_0^\tau \langle\tilde{\psi}| \frac{d}{dt} |\tilde{\psi}\rangle \, dt. \tag{2.30}$$

By appropriately choosing $f(t)$, for every curve C satisfying $\Pi(C) = \hat{C}$, one can choose same $|\tilde{\psi}(t)\rangle$. Therefore for a closed curve $\hat{C}$, the phase β does not depend on ϕ and H. From eq. 2.30, β does not depend on time t either. So it is purely geometrical.

In Aharonov and Anandan's original paper, three examples were discussed. First example is a spin $\frac{1}{2}$ particle in homogeneous magnetic field in the $\hat{\mathbf{z}}$ direction. In this case the Hamiltonian is given by

$$H_1 = -\mu B \sigma_z, \tag{2.31}$$

where

$$\sigma_z = \begin{bmatrix} 1 & 0 \\ - & -1 \end{bmatrix}. \tag{2.32}$$

The initial quantum state at $t = 0$ is given by

$$|\psi(0)\rangle = \begin{bmatrix} \cos(\theta/2) \\ \sin(\theta/2) \end{bmatrix}, \tag{2.33}$$

such that at a later time t,

$$|\psi(t)\rangle = \exp(i\mu Bt\sigma_z/\hbar)\,|\psi(0)\rangle = \begin{bmatrix} \exp(i\mu Bt/\hbar)\cos(\theta/2) \\ \exp(-i\mu Bt/\hbar)\sin(\theta/2) \end{bmatrix}. \tag{2.34}$$

This means the spin precesses with spin direction at the angle of θ to $\hat{\mathbf{z}}$. The spin precession period is $\tau = \pi\hbar/\mu B$. By using eq. 2.30, for every cycle, one has

$$\beta = \pi(1 - \cos\theta) + 2\pi n. \tag{2.35}$$

This result also means geometric phase exists naturally in quantum theory as one of the fundamental natures.

A second example AA discussed was similar to Berry phase on the point that $|\psi(t)\rangle$ is always the eigenstate of Hamiltonian $H(t)$ but with adiabatic approximation not satisfied. The third example is Aharonov-Bohm effect which could also be expressed as AA phase [2].

After AA proposed the non-adiabatic geometric phase theoretically, some experimental works were performed to observe it. Suter et al used NMR techniques to study a quantum system composed of coupled protons with total spin $J = 1$[81]. The Hilbert space is 3-dimensional because three independent states exist. Through a varying magnetic field, the geometric phase was observed by measuring the interference between two states and a third unperturbed one. Another experiment was performed by Chiao et al who used polarized light passing through a optical fiber which was helically twisted [25, 85]

For mesoscopic electronic system, some theoretical work concentrated on the geometric phase with the electron spin put into consideration. Ady stern analyzed a

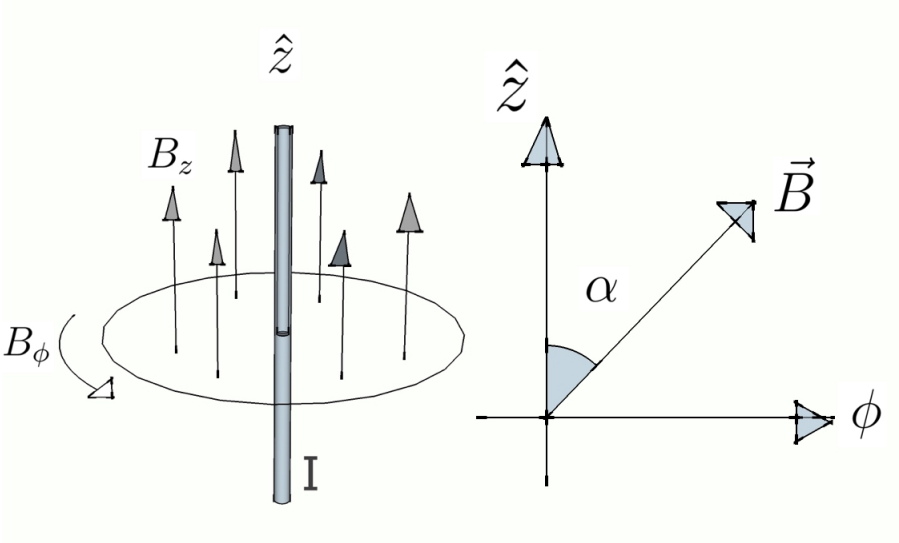

Figure 2.6 Stern analyzed the mesoscopic ring in the existence of inhomogeneous magnetic field composed of B_z and an azimuthal component B_ϕ. The ratio of two field components is defined by angle α [79].

ring in magnetic field which has both $\hat{\mathbf{z}}$ component and $\hat{\boldsymbol{\phi}}$ azimuthal components as shown in figure 2.6. In his work, the non-adiabatic condition for such a mesoscopic ring was analyzed in details [79]. Stern found the geometric phase can induce motive force which couples to spin.

Loss et al analyzed motion of electrons in a mesoscopic ring with a crown like magnetic field with $\hat{\mathbf{z}}$ component and polar $\hat{\boldsymbol{\rho}}$ component as shown in figure 2.7 [63]. They found Zeeman interaction between magnetic field and electron spin can couple the electron spin and orbital motion and lead to geometric phase. They also found persistent equilibriium charge and spin currents in the ring. Gao et al and Yi et al made detailed calculation for the mesoscopic ring with different inhomogeneous magnetic field texture [34, 94].

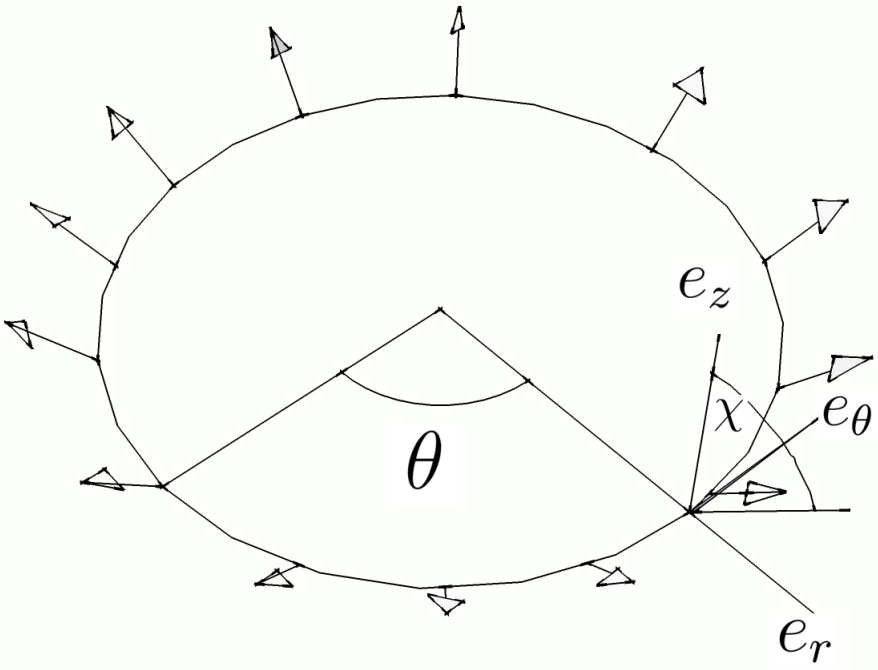

Figure 2.7 Loss et al analyzed geometric phase in mesoscopic ring with inhomogeneous magnetic field with both $\mathbf{e}_z$ component and polar $\mathbf{e}_r$ component. The angle between two components is χ [63].

Chapter 3

Quantum Phase Coherent Transport in Mesoscopic Thin Films

As mentioned in Chapter 1, conduction electrons transport in metal can be described with Drude's model which can give a simple illustration and good estimates of electronic properties within the classical picture [8]. With electric field applied, electrons conduction can be expressed as

$$J = \sigma E, \tag{3.1}$$

where J is electric current density, σ is conductivity which can be given as

$$\sigma = \frac{ne^2\tau}{m^*}, \tag{3.2}$$

where n is electron density, m^* the electron effective mass and τ the electron relaxation time. The mean free path which measures the average distance that an electron travels between scattering or collisions is given by

$$l = v_F\tau, \tag{3.3}$$

where v_F is the Fermi velocity. The corresponding Fermi wavelength is λ_F, which is also the de Broglie wavelength characterizing the Fermi gas.

In disordered metal, the electrons' trajectory is a random walk with average length scale of the mean free path. The scattering which leads to random walk comes from many sources such as impurities, defects, grain boundaries, phonons etc. These different types of scattering are usually categorized as elastic scattering and inelastic scattering with their corresponding relaxation time as τ_0 and τ_i. The elastic scattering

only changes the momentum of an electron while the inelastic scattering changes the energy of an electron. Therefore, τ_0 and τ_i are also the lifetime of an electron in its momentum eigenstate and energy eigenstate respectively.

3.1 Characteristic Length and Diffusive Transport

At low temperatures, the electron phonon inelastic scattering is suppressed. Therefore the conduction electron can maintain its phase coherence after experiencing many elastic scattering events. Both Aharonov-Bohm effect and weak localization effect observed at low temperature are such quantum phase coherence effect. For mesoscopic regime, the classical picture of conductivity can no longer give an adequate description. The wave nature of the electron also need to be put into consideration. In order to analyze the transport properties of electrons in mesoscopic structures, several characteristic length scales need to be identified and compared.

The elastic mean free path $l_0 = v_F\tau_0$ is a characteristic distance an electron's momentum is changed by elastic scattering centers such as impurities, defects and boundaries. Such elastic scattering does not break the phase coherence of electron wave function. So an electron can experience many elastic scattering before it loses its phase coherence.

Another length scale is the phase coherence length l_ϕ, which is defined as the distance between two complementary scattering events that an electron loose its phase coherence. The phase breaking sources include electron-phonon scattering and electron-electron scattering which are both inelastic scattering. At low temperature the scattering from phonon is negligible. Electron-electron scattering mainly contributes the phase breaking.

By comparing the sample length L and width W with elastic mean free path l_0 and phase coherence length l_ϕ, one can clearly distinguish the different transport regimes as shown in figure 3.1:

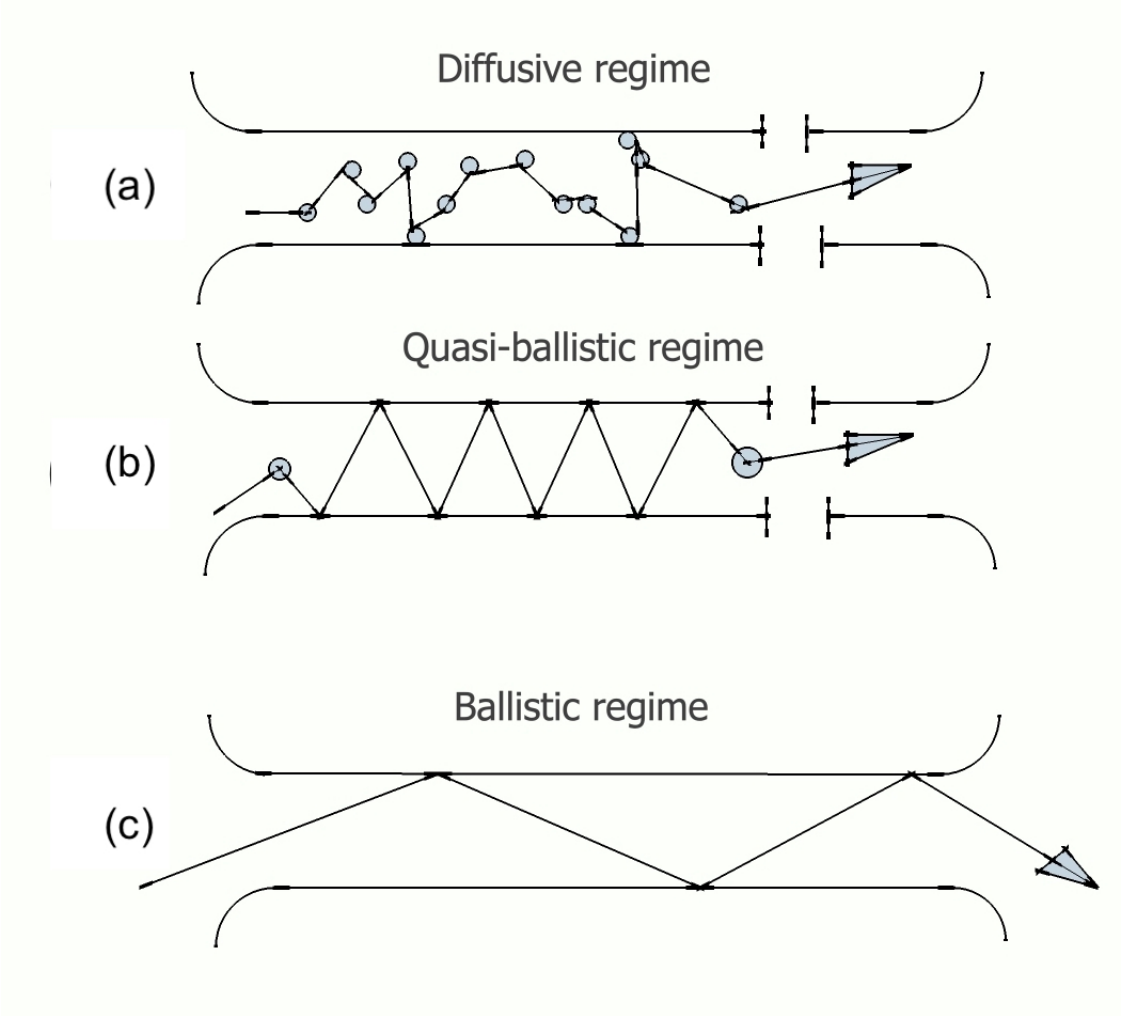

Figure 3.1 Schematic diagram for different electron transport regimes: diffusive regime; Quasi-ballistic regime; ballistic regime [42].

Ballistic regime: $l_\phi \gg l_0 \gg L, W$:

In ballistic regime, the sample size is much smaller than the elastic mean free path. Therefore the electrons encounter almost no scattering from impurities. The dominant scattering is from the boundaries of conductor. The time of flight is $\tau_f = L/v_F$ with electron momentum assumed to be constant. Additionally, if the width of sample is small compared to λ_F, there are only several channels for the electron transport [59].

Quasi-ballistic region: $W < l \ll L$

Diffusive regime: $L, W \gg l_0$.

In diffusive regime, the elastic mean free path is much smaller that the length of the sample. The disorder scattering dominates. Therefore the electron performs random walk. When phase coherence is taken into account, the situation is more interesting. In diffusive region, the phase coherence length can be expressed as:

$$l_\phi = \sqrt{D\tau_\phi}, \tag{3.4}$$

where D is the diffusion coefficient of electrons in the conductor, τ_ϕ the dephasing time.

In the weakly disordered diffusive regime, i. e. $\lambda_F \ll l_0 \ll L, l_\phi$ mesoscopic regime, many interesting quantum phase coherence phenomena such as AB h/e oscillation, AAS $h/2e$ oscillation and weak localization effect will appear.

3.2 Altshuler-Aronov-Spivak $h/2e$ Oscillation and Weak Localization: Coherent Backscattering

As mentioned in Chapter 1, Aharonov-Bohm effect of h/e oscillation observed in sub-micron diameter Au ring is a typical evidence of quantum phase coherence for the sample size comparable to l_ϕ. However, the magnetoresistance oscillation measured with a lithium cylinder showed $h/2e$ oscillation as shown in figure 3.2 [5, 6]. Similar AAS $h/2e$ oscillation was also observed in a series of arrays of sub-micron diameter silver loops (one, three, ten and thirty) as shown in figure 3.3a* [87]. Both metal cylinder and ring arrays can be interpreted as ensemble of identical and uncorrelated rings. Umbach et al's work clearly showed $h/2e$ oscillation can persist for ensemble average of many loops while the h/e AB oscillation decreases linearly with square root of the number of loops as shown in figure 3.3b* [87]. This means the phase coherent $h/2e$ AAS oscillation can persist on average while h/e AB effect can not. Another significant difference between h/e AB oscillation and $h/2e$ AAS oscillation is

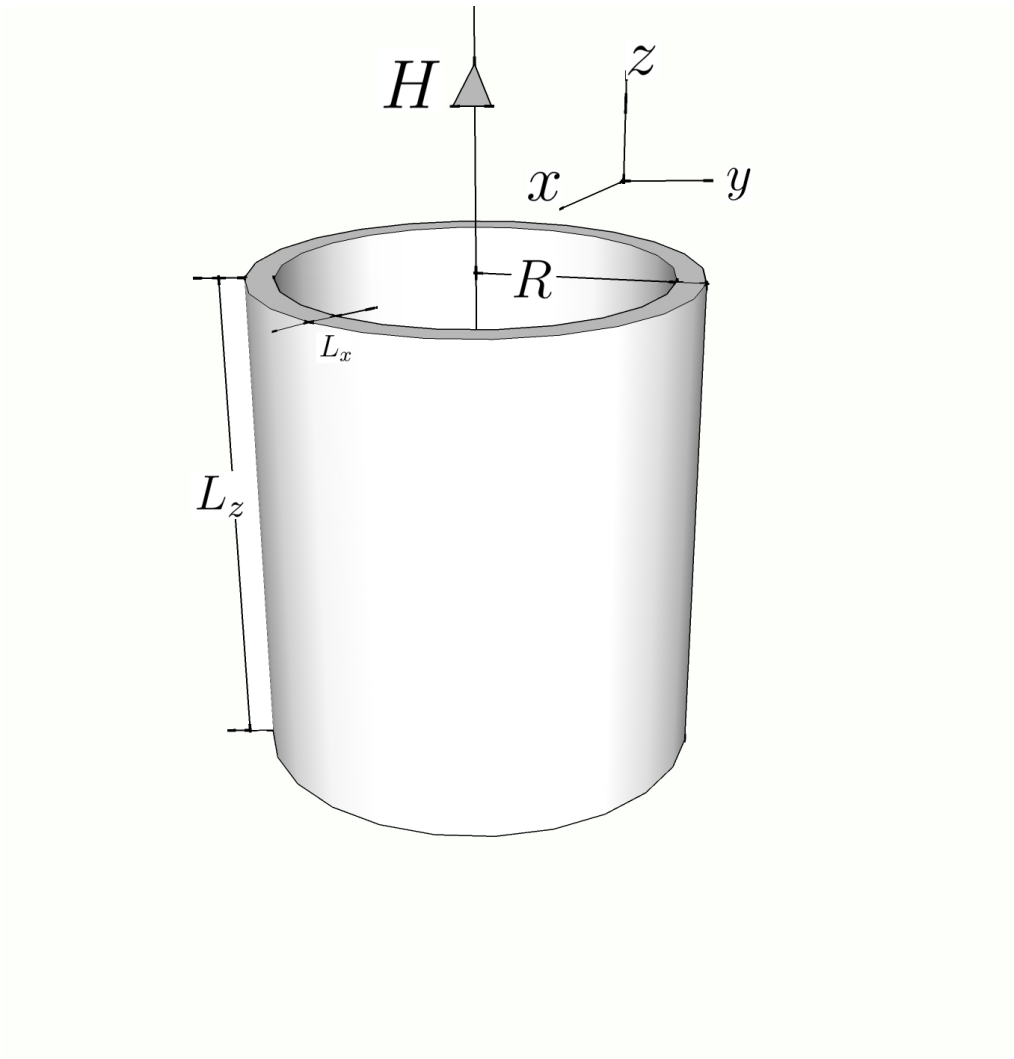

Figure 3.2 Lithium film evaporated on a quartz filament. L_z is 1cm, l_ϕ is 2.3μm, film thickness is 0.12 μm. The diameter is 1.1 μm. $h/2e$ magnetoresistance oscillation was observed with lithium cylinder from [5, 6].

that $h/2e$ oscillation only exist at low magnetic field while h/e oscillation can persist to rather high magnetic field [91, 23, 87].

It is also found that $h/2e$ oscillation is superimposed on a background magnetoresistance change which also appear in single metal wire [87, 23, 5, 6]. This background magnetoresistance change is known as weak localization (anti-localization) correction which will be discussed later. These natures of AAS effect can be explained as originating from coherent backscattering of two electron partial waves that propagate in

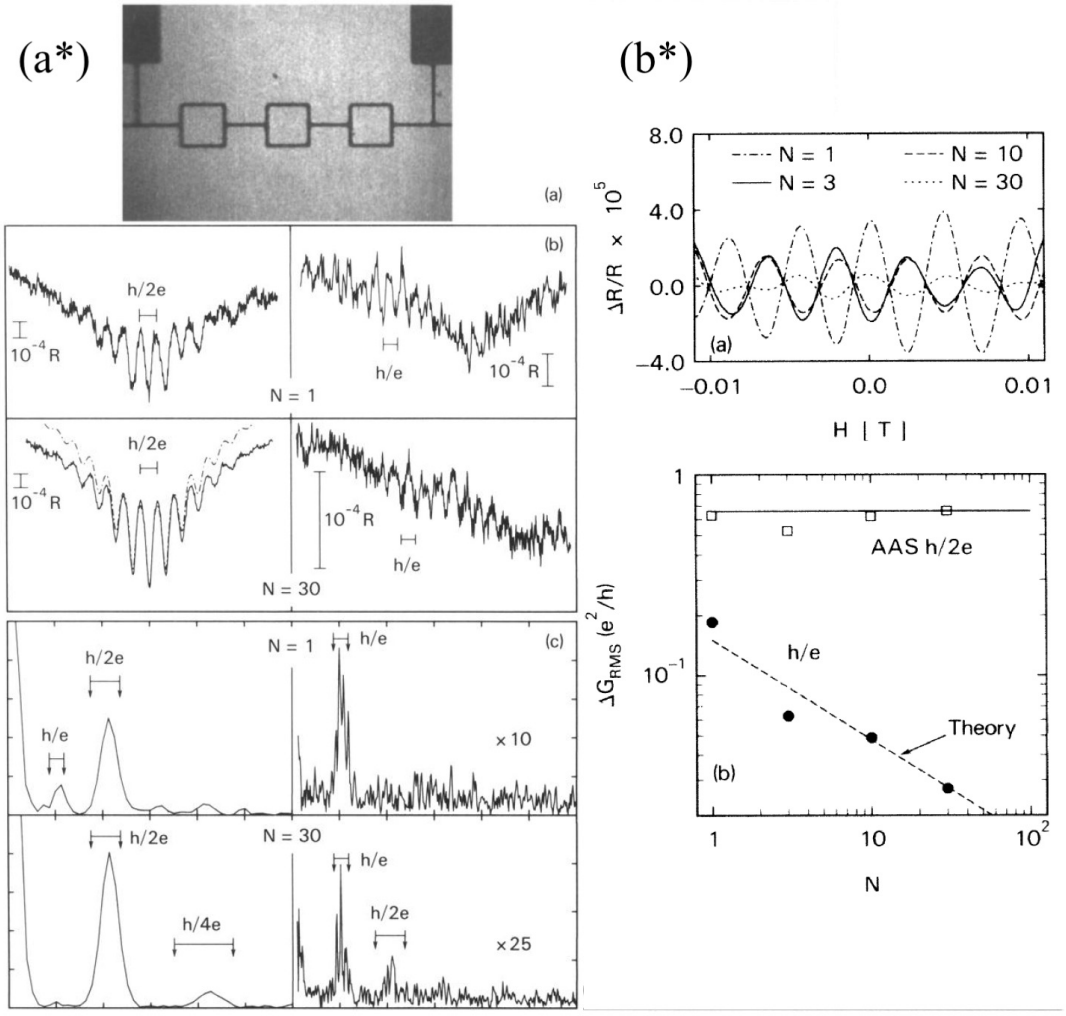

Figure 3.3 a*, h/e and $h/2e$ magnetoresistance observed in one, three and thirty silver loops. b*, $h/2e$ oscillation persists with increasing number of loops. h/e oscillation decrease linearly with the square root of number of loops[87].

opposite directions along time reversal trajectory.

Here both h/e oscillation and $h/2e$ oscillation will be analyzed.

Landauer electrical theory tells that the electrical conductance is related to transmission probability as

$$G = 2\frac{e^2}{h}T. \tag{3.5}$$

Therefore the measured conductivity oscillation actually reflects the electron wave transmission probability oscillation.

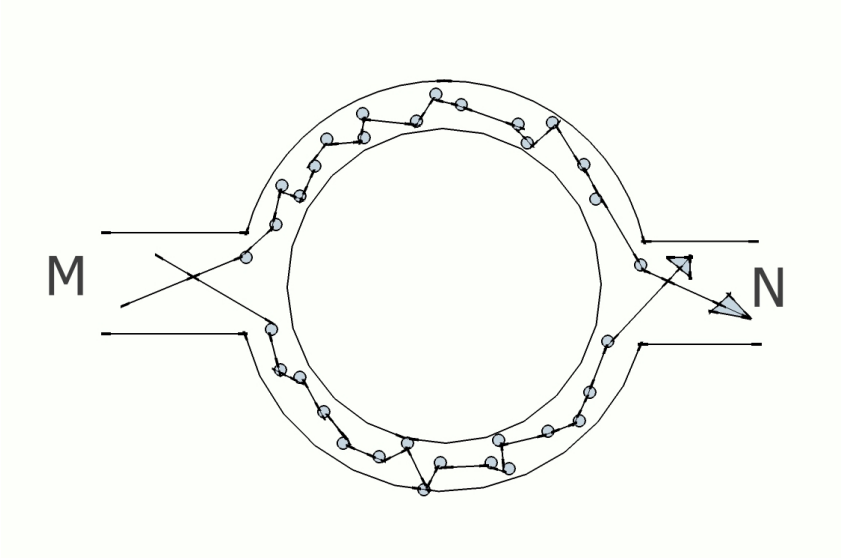

Figure 3.4 Schematic diagram of the ring with disordered scattering center. Electron transverse from position M to position N through two Feynman paths.

For simplification, let's consider the one dimensional ring structure first. Considering an electron transmitted from position M to position N as shown in figure 3.4. The electron wave Ψ is decomposed into two partial waves $\psi_j = t_j e^{\phi_j}$ $(j = 1, 2)$, where t_j is the amplitude of two partial waves. Two partial waves traverses the top and bottom arms respectively through many elastic scattering centers and form two Feynman paths. The total transition amplitude at position N is

$$\Psi(N) = \sum_j \psi_j = \sum_j t_j \exp(i\phi_j) \tag{3.6}$$

The probability to find the electron at position N with flux Φ is

$$P(N) \equiv |\Psi(N)|^2 = \sum_j |\psi_j|^2 + \sum_{j \neq k} |t_j||t_k| \cos(\phi_j - \phi_k). \tag{3.7}$$

Where the first term is classical transition probability, the second term denote the interference effect. With Φ applied, specifically for the ring, the electron canonical momentum is $\mathbf{p} + e\mathbf{A}/c$ considering the electron charge of $-e$, the phase change of the j trajectory is

$$\phi_j = \phi_j^{(0)} + \frac{e}{\hbar} \int_1 \mathbf{A} \cdot \mathrm{d}\mathbf{l}, \tag{3.8}$$

where $\phi_j^{(0)}$ is the phase when $\Phi = 0$. For the ring with $j = 1, 2$, the phase change in the interference term is

$$\Delta\phi(\Phi) = \phi_1^{(0)} - \phi_2^{(0)} + \frac{e}{\hbar}\oint \mathbf{A}\cdot \mathrm{d}\mathbf{l} = \Delta\phi^{(0)} + 2\pi\frac{\phi}{\phi_0}, \tag{3.9}$$

where $\phi_0 = h/e$, which gives the Aharonov-Bohm conductance oscillation while changing B field and the relevant flux Φ with period of h/e.

It is generally understood that in equation 3.9, $\Delta\phi^{(0)}$ is a random phase between $-\pi$ and π when the flux Φ is 0 [70, 47]. There are several possible reasons for the random 0 flux phase. One reason is for a specific single ring, the microscopic details of trajectory 1 and trajectory 2 are different. Electrons experience different scattering events while traversing through trajectory 1 and 2, leading to a random phase. The second reason is at beam splitter N, a fraction of the wave coming from the half ring does not leave the ring but travers back around another half ring. This lead to either 0 or π random phase form more complete calculation [41]. Because of this 0 flux random phase for specific ring, while taking ensemble average over rings arrays as in Umbach et al's work or ensemble average of the long cylinder as in Sharvin Sharvin's work, the h/e oscillation which comes from the second term of equation 3.7 dies out.

Now it is the turn for $h/2e$ AAS oscillation which can survive ensemble average. In AB oscillation, the two trajectories are half circle as shown in figure 3.5a. However, there is another possibility that two partial waves can traverse the whole ring and finally interfere at the origin point supposing the phase coherence is mainteined. Let's re-write the transition probability at original point

$$P(M) \equiv |\Psi(M)|^2 = \sum_j |\psi_j|^2 + \sum_{j\neq k} |t_j||t_k| \cos(\phi_j - \phi_k). \tag{3.10}$$

In this case, with the applied flux, the phase change in the interference term is

$$\Delta\phi(\Phi) = \phi_1^{(0)} - \phi_2^{(0)} + 2\frac{e}{\hbar}\oint \mathbf{A}\cdot \mathrm{d}\mathbf{l} = \Delta\phi^{(0)} + 4\pi\frac{\phi}{\phi_0}. \tag{3.11}$$

Therefore the interference term contributes an oscillation of $h/2e$ to the conductance. If the two trajectories are time reversed paths, which means the trajectories are

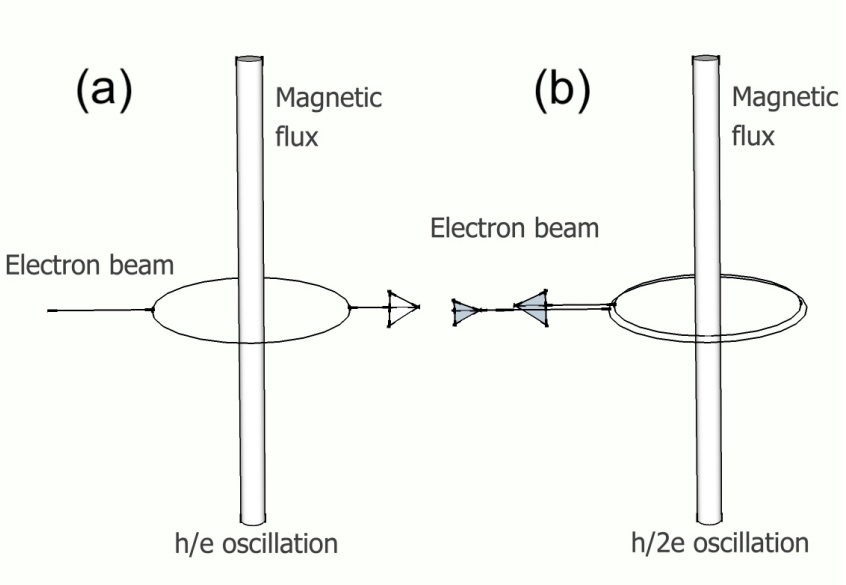

Figure 3.5 a, Two partial waves traverse along half circle and interfere with each other. b, Two partial waves traverse in opposite direction encircling the whole ring and satisfying time reversal symmetry. The interference happens at the origin point. [47].

exactly identical (electrons scatter from the same impurities) but only in opposite directions, the random phase $\Delta\phi^{(0)}$ disappears. This process is often recognized as Coherent Back Scattering. The time-reversed pairs are often called Cooperons due to the similarity to superconducting Cooper pairs [60].

When ensemble average is taken for ring arrays as in figure 3.3 or figure 3.2, every ring contribute an $h/2e$ oscillation with 0 random phase. This is why the AAS oscillation can survive the ensemble average, which is a major difference with AB oscillation.

From experiment it was found that AAS $h/2e$ oscillation only appears at low magnetic field, the oscillation amplitude decreases with increasing magnetic field. This is because as field increases, the Lorentz force coming from the magnetic field penetrating the ring arms breaks the time reversal symmetry of the two trajectories of Cooperons.

Another quantum coherent interference effect is weak localization correction to conductivity observed in disordered diffusive metal thin film or wire at low temperature. When $\Phi = 0$, the probability of the electrons to return back to the origin is enhanced because of the Coherent Back Scattering. This is the origin of Weak Localization. It also happens in quasi-one dimensional metal wires or two dimensional metal thin films. It can be understood as there exists many coherent back scattering loops with different area the loops encircle. While a magnetic field is applied, the time reversal symmetry of the coherent back scattering loops is broken, therefore the conductance is increased (for the case of weak spin-orbit coupling). For the case of strong spin orbit coupling, the coherent back scattering contributes destructive interference of the back scattered probability by flipping the spin direction and leads to the opposite weak anti-localization.

Chapter 4

Sample Fabrication and Electrical Measurements

4.1 Electron Beam Lighography

Electron beam lithography is a very effective way for the nano scale fabrication. In our experiment, sequential E-Beam lithography is heavily used for the fabrication of multilayer structure. The reason we chose such a difficult way to make NLSV is because we wanted to realize single layer everywhere but not only the center small feature, such that the possible more intrinsic nature of NLSV can be measured and analyzed. Most of the sample fabrication procedure is completed in the cleanroom.

We used a <100> N-type silicon wafer with thermally oxidized SiO_2 layer on top. The wafer was pre-cleaned by ultrasonic cleaning in acetone for 3 minutes, then in isopropyl alcohol (IPA) for 3 minutes. Then the wafer was blow dried with pure nitrogen gas.

1, The wafer first spin coated a layer of PMMA 495 for 45 seconds.

2, Then the wafer was baked on a hot plate with temperature of 180°C for 90 seconds in the fume hood.

3, The wafer was spin coated with another layer of PMMA 950 for 45 seconds for 45 seconds.

4, Then bake the wafer on a hot plate with temperature of 180°C for 90 seconds in the fume hood. Cautions need to be taken to prevent dust from accumulating on the PMMA.

5, The wafer was then put in SEM for E-beam lithography. JEOL JSM-840A and Zeiss ultra plus were used to write the pattern. For JEOL JSM-840A, the sample pattern was first designed with Design CAD, then converted to DC2 files and layer files. Through the AD converter, the SEM write the layers of pattern on the wafer. For the Zeiss ultra plus FESEM, the patterns were also first designed with Design CAD. Then the JC Nabity Nanometer Pattern Generation System (NPGS) was used for focusing, optimizing the SEM and writing the pattern with the run file with parameters such as dose, line spacing etc. Usually 12 samples with different ring diameter or injector detector distance were fabricated on a single piece of wafer to get samples with uniform nature. The sample patterns and alignment marks were written together on the wafer.

6, The wafer was taken out of SEM and put into developer (MIBK : IPA = 1 : 3) for 30 seconds and then rinsed with isopropyl alcohol (IPA) and blow dried with pure nitrogen gas.

Then the wafer was ready for metal and oxide deposition. For Al/MgO/Co samples, the Al/MgO ring and bar spacer layer was patterned and deposited first. Then a second E-beam lithography was performed to pattern and deposit the Co layer. For Py/MgO/Al samples measured in dilution fridge, the Py/MgO injector and detector bars were patterned and deposited first via magnetron sputtering, followed by second E-beam lithography and deposition of Al rings and bars.

4.2 Thermal, E-Beam Evaporation and Magnetron Sputtering Deposition

The wafer was then put into Torr International combination deposition chamber and pump down to 10^{-7} Torr. For Al/MgO/Co sample, 200 nm Al layer was first evaporated from 99.999% purity aluminum pellets which were heated in a Al_2O_3 coated tungsten boat. Then without breaking the vacuum, RF magnetron sputtering

was used to deposit 2 nm MgO layer from MgO target with working gas of high purity Argon. After the second layer E-beam lithography pattern, 50 nm Co layer was deposited by thermal evaporation or e-gun evaporation.

For Py/MgO/Al samples, the wafer was put in AJA International Sputtering system for deposition. With all the needed targets installed, the system was first pumped down to base pressure of 10^{-8} Torr. Sometimes, in order to accelerate the pumping, the quartz heater was used to bake the whole chamber. Deposition rate and corresponding sputtering time were first checked with film thickness monitor. Then the wafer was transferred in the main chamber. The substrate which hold the wafer was spinning at 12 revolutions per minute to get uniform film thickness. Before actual deposition, all targets were pre sputtered for several minutes to remove the possible contamination or oxide layer on the surface. 20 nm Py layer was first sputtered on the wafer. Then the MgO layer with thickness of 2 nm was sputtered on top.

After sputtering, the sample was taken out for lift-off in acetone. Then the wafer was spin coated with PMMA 495 and 950 again for the second step e-beam lithography and Al spacer sputtered deposition.

4.3 Other fabrication steps: dry etching, dicing and wire bonding

Before the second layer deposition, Argon plasma was used to remove the possible contamination or developer residue, either in the Trion RIE/ICP dry etch system or in the sputtering chamber.

After the two step lithography and deposition, 12 samples on the wafer were divided into 12 parts by wafer dicing. Then each small piece of wafer with one sample on it was glued on the sample holder with silver paint.

At last, wire bonding was performed to connect the 6 contacting pads of the sample to the leads of the sample holder. Either Au or Al wires were used for wire bonding.

The sample was ready for measurement in PPMS or dilution fridge.

4.4 Physical Property Measurement System: electrical measurement at low temperature

The electrical properties of Al/MgO/Co samples were measured in Quantum Design Physical Property Measurement System (PPMS) equipped with 9 Tesla superconducting magnet. The lowest temperature the PPMS can reach is 1.9 K. Sample holder was mounted on a probe with rotator such that the angle between magnetic field and sample plane can be changed from 0 to 90 degree. After setting the temperature of sample chamber of PPMS at 305 K, the rotational probe with sample was inserted in the sample chamber, then purged with Helium gas for 3 times and pumped down to 10 mTorr. Then the temperature was drop to the desired temperature such as 4.2 K and 1.9 K for Non-local voltage measurement with parallel and perpendicular magnetic field sweep. The probe leads connecting the sample were connect out to a home made switch box such that the more accurate Stanford Research System Lock-in Amplifier SR 850, 8.5 digit multimeter and AC/DC current sources could be used for electrical measurement. All connecting leads out of the PPMS were well shielded. Military species connector was used to secure shielding.

4.5 Dilution Refrigerator for Milli-Kelvin Measurement

Another group of Py/MgO/Al samples were taken to National High Magnetic Field Laboratory for milliKelvin temperature measurement in Oxford dilution refrigerator with parallel sample stage and perpendicular sample state.

Chapter 5

Simultaneous Detection of Spin Signal and Interference

The Aharonov-Bohm (AB) effect was first proposed in 1959 and experimentally observed in 1985 in a mesoscopic Au ring by electrical quantum phase coherence detection of h/e oscillations during magnetic field sweeps at very low temperature [3, 91]. The wavefunction phase change due to the AB effect was later reformulated by Berry as a special case of his Berry phase in 1985 [16, 7]. Berry considered an adiabatic geometric phase in which the quantum system is always in an instantaneous eigenstate and whose Hamiltonian changes adiabatically around a closed circuit in parameter space [16, 19]. Aharonov and Anandan (AA) later proposed a more generalized geometric phase for non-adiabatic evolution where the quantum state need not be an eigenstate of the Hamiltonian [7, 2].

In a mesoscopic metal ring structure with interaction between spin and external magnetic field included, the quantum adiabatic approximation is valid for eigenstates in which the spin direction is parallel or antiparallel to the magnetic field and for fields at which the time it takes the electron to transit the ring is much larger than the period of Larmor precession [79, 32, 43].

We design and fabricate, for the first time, a non-local lateral spin valve (NLSV) electron interferometer with such a ring structure. We experimentally observe AA's non-adiabatic geometric phase by measuring both the coherent h/e oscillation and spin precession. Spins were injected aligned in plane with the ring and the magnetic

field was perpendicular to it. The field was low to ensure that the precession time was longer than the transit time of the ring, resulting in non-adiabatic transport, and therefore making this an AA phase measurement rather than a Berry phase measurement.

A NLSV is an effective tool to generate and detect spin polarized electrons in mesoscopic metal and semiconductor systems. In Hanle effect measurements, a magnetic field perpendicular to the plane generates spin precession with a spin direction in plane while electrons diffuse from injector to detector [96, 36, 50, 84, 33, 38, 64, 26, 39]. During diffusion, spin can relax via ordinary momentum scattering with spin-orbit coupling [96], i.e. the Elliot-Yafet mechanism. Momentum scattering in diffusive metal films is typically caused by impurities [15]. Such scattering is elastic and therefore does not break the phase coherence of the electron wave function. Electron-phonon inelastic scattering is the main cause of phase decoherence. But at low temperatures, this is suppressed, thereby enabling the observation of interference effects like those due to weak localization and AB oscillations even in disordered diffusive metals [91, 15]. However, in the original AB effect measurement in Au rings, spin was not considered, nor was the spin-magnetic field interaction from the field that penetrates the ring itself [91].

5.1 Non-local spin Signal and distance dependence

Figure 5.1a shows a sketch of the interferometer. Ferromagnetic bars FM1 and FM2 serve as spin injector and detector. FM1 and FM2 spacing l is relatively large to fit the ring between them. In order to get a large non-local spin signal for such a large spacing, several factors need to be considered [46]. Assuming an Elliot-Yafet mechanism, the spin-orbit coupling in combination with momentum scattering leads to spin relaxation [96], while spin-orbit coupling is generally believed to be proportional to the fourth power of the atomic number of the metal [78]. Therefore we use aluminum,

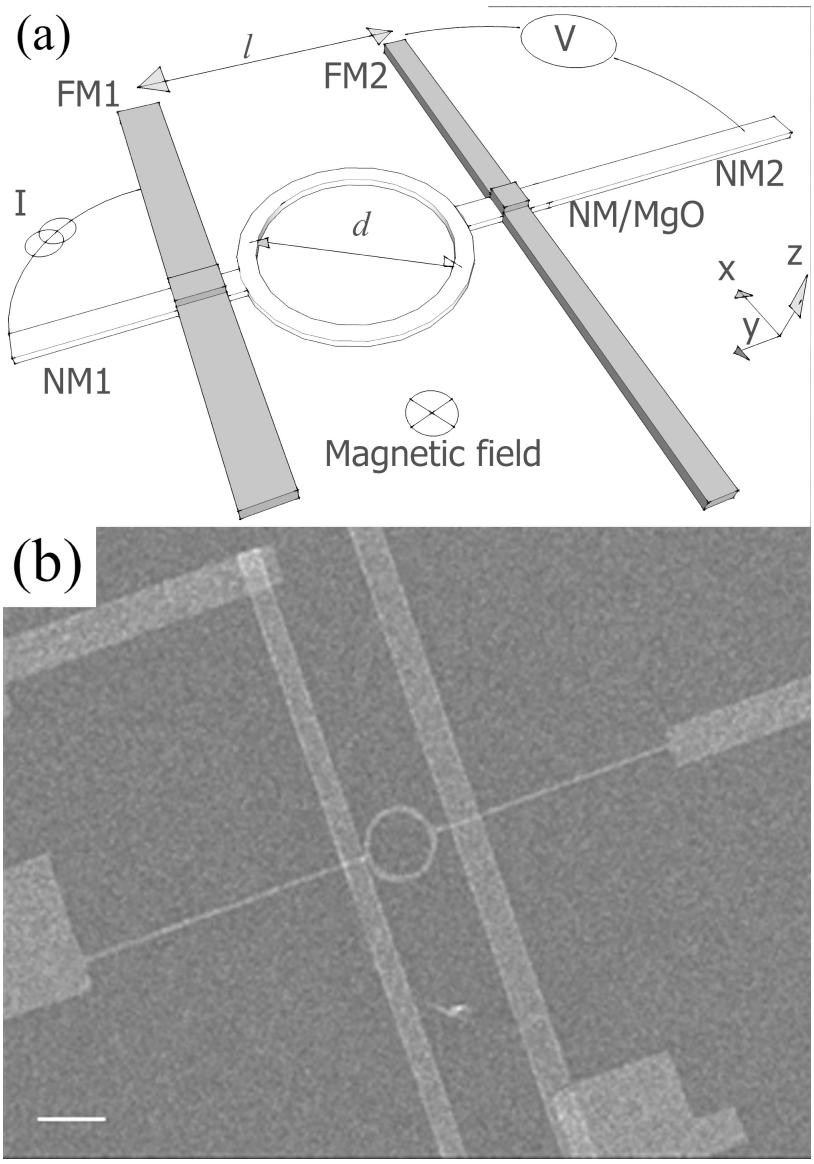

Figure 5.1 (a) Sketch of the NLSV interferometer. Ferromagnetic bars FM1 and FM2 with moments parallel and in plane. AC current was applied between FM1 and NM1. With perpendicular magnetic field, the precessing spin current diffuses from FM1 to FM2 while experiencing a non-zero magnetic potential due to the magnetic flux enclosed by the ring. Non-local voltage is measured between FM2 and NM2. The distance of electron transport from FM1 to FM2 is $L = l + (\pi/2 - 1)d$. (b) SEM image of Al/MgO|Co NLSV after electrical measurement. The scale bar is 1 μm. The diameter of the Al/MgO ring is 0.95 μm while the line width of the ring is 100 nm $\pm$ 20 nm. Different profiles of Co1 (0.4 μm wide and 18 μm long) and Co2 (0.3 μm wide and 28 μm long) give different coercive fields.

which has the advantage of a relatively large spin diffusion length of 1.2 μm [46, 51] and large phase coherence length of 2.0 μm [23]. It has also been reported that a MgO tunnel barrier can enhance spin accumulation, by reducing the conductance mismatch between the FM and NM, and therefore enables long distance spin precession [33, 38]. Therefore, we constructed Al/MgO|Co(Py) NLSVs with ring-shaped NM spacers.

Figure 5.1b is an SEM image of a Al/MgO|Co device with 0.95 μm diameter ring. Two separate e-beam lithographic and deposition phases were required to build the samples. First, the NM ring and electrodes were patterned by e-beam lithography and 20 nm of Al was deposited by thermal evaporation at a base pressure of 10^{-7} Torr. Without breaking vacuum, 2 nm of MgO was deposited via RF magnetron sputtering. Second, e-beam lithography was again used to pattern the FM bars and, before metal evaporation, an Argon plasma was used to remove any lithographic residue and other contamination. Then, 50 nm of Co was thermally evaporated at 10^{-7} Torr. Finally, samples were annealed at 360 °C for 10 minutes at 10^{-6} Torr [95].

For the samples considered here, the diameter d of the rings, measured via SEM, were 0.95 μm and 2.2 μm. Electron transport distance L was 2 μm for 0.95 μm ring. Al bar samples with L of 0.5 μm, 1 μm and 2.3 μm were also fabricated at the same time to serve as controls. Al/MgO|Co samples were measured in a cryostat with a lowest achievable temperature of 1.9 K. Another group of Py(20 nm)/MgO(2 nm)|Al(60 nm) ring samples were fabricated and measured in a dilution refrigerator with a lowest achievable temperature of 50 mK.

We first measured non-local voltage V_{NL} for both ring and bar samples with different L using standard lock-in techniques. Alternating current, amplitude of 2 μA at 17 Hz, was applied between Co1 and NM1. V_{NL} was measured between Co2 and NM2. The in-plane field, $B_{\|}$, was swept between $\pm$0.03 T at 1 mT/s and 4.2 K. The inset of figure 5.2 is a typical non-local spin current measurement for the 0.95 μm

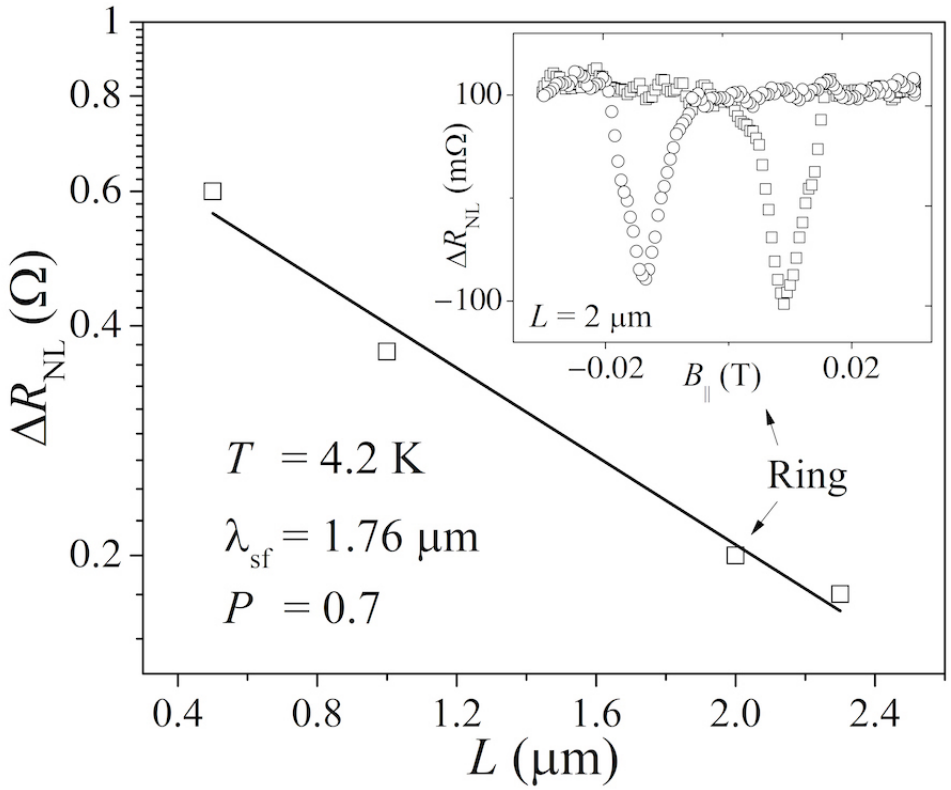

Figure 5.2 Spin resistance for In-plane magnetic field: Distance dependence of spin resistance for both ring ($L = 2$ μm) and bar samples ($L = 0.5$ μm, 1.0 μm and 2.3 μm) at 4.2 K yields an average spin diffusion length of 1.76 μm and spin polarization rate of 0.7. Inset: 200 mΩ spin resistance was observed for a 0.95 μm ring with 2 μm Co1/Co2 distance.

ring. A very high spin resistance ($\Delta R_{\rm NL} = \Delta V_{\rm NL}/I$) of 200 m$\Omega$ was observed for $L = 2\mu$m.

Spin resistance and diffusion length are related by[50]

$$\Delta R_{\rm NL} = \pm\frac{1}{2}P^2\frac{\lambda_{\rm sf}}{\sigma_{\rm Al}A}\exp(-L/\lambda_{\rm sf}). \tag{5.1}$$

P is the spin polarization of current injected into Al from Co1, $\lambda_{\rm sf}$ the spin diffusion length in the Al, and A the cross sectional area of the tunnel junction. $\sigma_{\rm Al}$ is the conductivity of the Al film which was found to be 3×10^7 Ω^{-1}m^{-1} from the linear

fit in figure 5.2. We find an average spin diffusion length of 1.76 μm and a spin polarization of 0.7 in both the ring and bar samples.

Theoretically, the channel width might affect spin resistance by introducing more space for random walk in diffusion, but actually for qusi-one-dimentional metal wires (width w, thickness t, length L, satisfy $w, t \ll \lambda_{sf}, w, t \ll L$), to what extend it can influence the spin resistance for metal wires in the ring sample is not clear (considering 1.49 μm long wire is doubled in width and the spin resistance of ring fits within error in the exponential decay of bar samples. This inspires an interesting experimental work of channel width dependence on spin resistance. If possible we will work that out in the future.

5.2 Hanle effect Measurement with Perpendicular Field

To determine the transverse spin diffusion length, a Hanle spin precession measurement was made with an out-of-plane magnetic field, $B_\perp$ between ± 0.17 T at 1 mT/s, for the same ring sample 1 in figure 5.2. The sample was first prepared in parallel configuration. Figure 5.3 shows the resulting Hanle effect curve. The solid line fits the spin resistance to [50]

$$\Delta R_{\mathrm{NL}} = \pm \frac{P^2}{e^2 N_{\mathrm{Al}} A} \int_0^\infty \mathrm{p}(t) \cos(\omega_{\mathrm{L}} t) \exp(-t/\tau_{\mathrm{sf}}) \mathrm{d}t, \tag{5.2}$$

where $\mathrm{p}(t) = (1/\sqrt{4\pi D t}) \exp\left[-L^2/(4Dt)\right]$ is the distribution of diffusion times from injector to detector, e the electron charge, D the diffusion coefficient in Al, $N_{\mathrm{Al}} = 2.4 \times 10^{-3}$ eV^{-1}cm^{-3} the density of states of Al near the Fermi level[71], $\omega_{\mathrm{L}} = g\mu_{\mathrm{B}} B_\perp/\hbar$ the Larmor frequency, and g the g-factor in Al. From the fit, we get a spin relaxation time of $\tau_{\mathrm{sf}} = 286$ ps, diffusion coefficient of 0.0108 m^{2}s^{-1} and spin polarization of 0.68. The spin diffusion length is then $\lambda_{\mathrm{sf}} = \sqrt{D\tau_{\mathrm{sf}}} = 1.69$ μm, which agrees quite well with the previous distance-dependent spin resistance measurements.

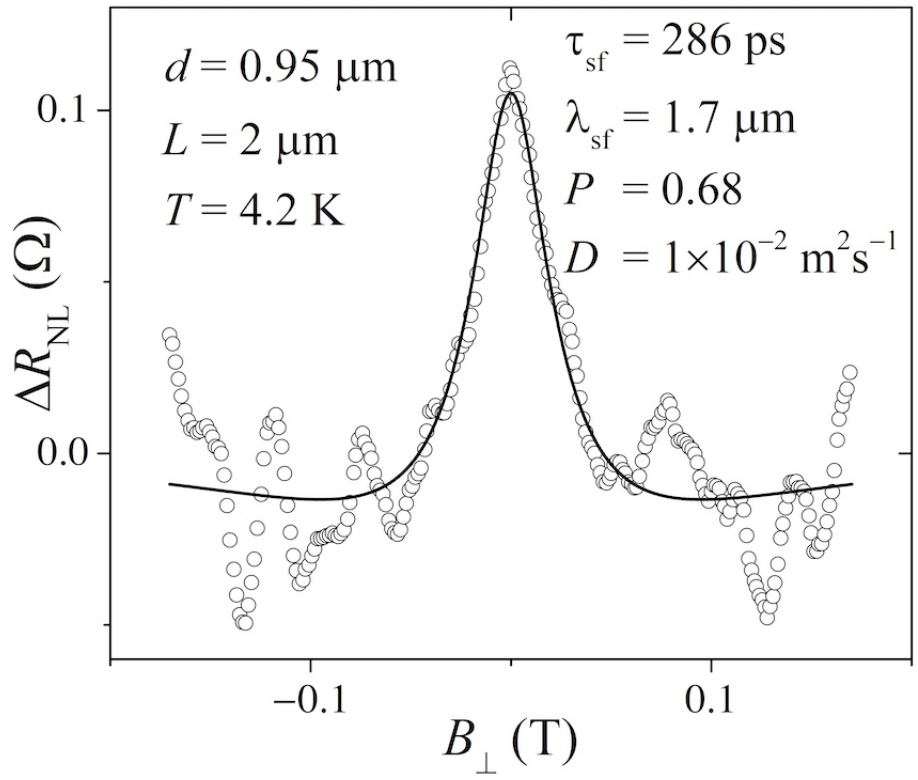

Figure 5.3 Spin resistance for perpendicular fields for ring sample 1: Black circles are data showing a clear Hanle effect curve for a 0.95 μm ring Al/MgO|Co at 4.2 K. Solid line is a least squares fit to eq. 5.2. Only every 10^{th} data point is shown for clarity.

5.3 Non-adiabaticity and Aharonov-Anandan Phase: Spin Current Aharonov-Bohm Oscillation

The Hamiltonian for an electron with spin is

$$H = \frac{1}{2m^*}\left[\mathbf{p} + \frac{e}{c}\mathbf{A}(\mathbf{r})\right]^2 + V(\mathbf{R}_n) + \mu\mathbf{B}\cdot\boldsymbol{\sigma}. \tag{5.3}$$

where m^* is the effective electron mass, $\mathbf{p} + \frac{e}{c}\mathbf{A}(\mathbf{r})$ its generalized momentum, $\mathbf{A}$ the magnetic vector potential, μ the electron magnetic moment, and $\boldsymbol{\sigma}$ the Pauli matrix. $V(\mathbf{R}_n)$ is defined by the confinement of the conductor and the impurity potential

[79, 34, 32, 94, 43], where $\mathbf{R}_n$ is the position vector of the n^{th} scattering event.

In the explanation offered in the experimental observation of AB phase in Au rings [91], electrons are assumed to move ballistically between elastic scattering centers $\mathbf{R}_i$ and $\mathbf{R}_{i+1}$. When the spin degree of freedom is not considered, $H(\mathbf{R}_i)\,|\psi_i\rangle = E(\mathbf{R}_i)\,|\psi_i\rangle$ holds after the scattering event at $\mathbf{R}_i$ such that $|\psi_i\rangle$ is the instantaneous eigenstate of eq. 5.3 without the last term. This is how the AB phase is viewed as a special case of Berry's adiabatic geometric phase [16].

The complete description of the electron quantum state is $|\Psi(t)\rangle = |\psi(\mathbf{r},t), \mathbf{S}(t)\rangle = |\psi(\mathbf{r},t)\rangle \otimes |\mathbf{S}(t)\rangle$, where $|\psi(\mathbf{r},t)\rangle$ is the spatial part while $|\mathbf{S}(t)\rangle$ is the spin part. The injector aligns the spins in the x-direction (figure 5.1a), i.e. $|\mathbf{S}(t=0)\rangle = |S_x;\pm\rangle$, the eigenstate of S_x. When diffusing from injector to detector through the ring with a uniform magnetic field $\mathbf{B} = B_z\hat{\mathbf{z}} = B_\perp\hat{\mathbf{z}}$ applied, the spin precesses in the x-y plane at the Larmor frequency.

The spin is perpendicular to B_z after each scattering event, so the electron state ket $\Psi(t)$ is not at the instantaneous eigenstate of the Hamiltonian, eq. 5.3, since $[H, S_z] = 0$. The average value of S_x can be inferred by the non-local voltage between Co2 and NM2 and the associated Hanle curve. At $B_z = 0$, the electrons diffuse from injector to detector without spin precession. When B_z increases to $B_{z,min} = 0.15$ T as shown in figure 5.4a, the Hanle curve reaches its first minimum, for which the spin precession angle is π [46].

Since half of the ring circumference is $\frac{1}{2}\pi d$, the magnetic field which causes a precession of π while diffusing a distance $\frac{1}{2}\pi d$ is $B_{z,\pi} = (2L/\pi d)B_{z,min} \approx 0.19$ T. Therefore, for magnetic fields $B_z < 0.19$ T, the time for an electron to transit the ring is shorter than the period of Larmor precession. Based on the above analysis, in 0.95 μm NLSV interferometer at low fields, the quantum adiabatic approximation is violated.

We use AA's approximate treatment to get the geometric phase factor[2],

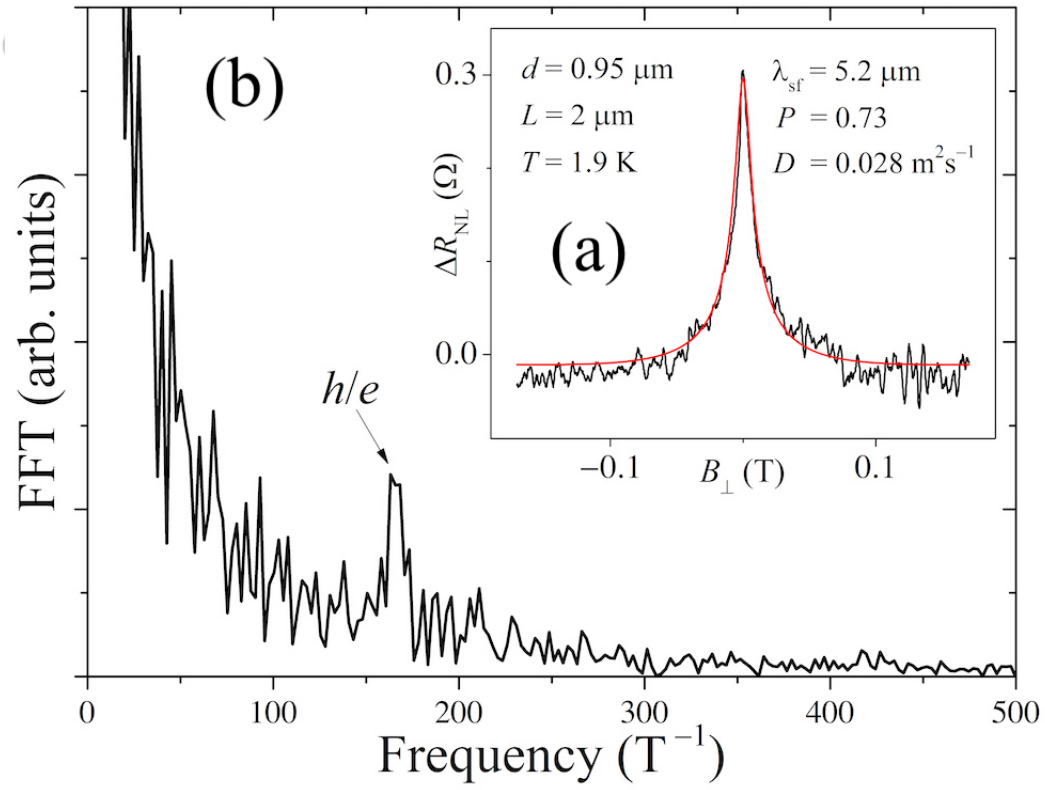

Figure 5.4 (a) Non-local Hanle curve for a 0.95 μm ring at 1.9 K. (b) FFT of the non-local Hanle curve shows a peak at 168 T^{-1}, which corresponds to an h/e oscillation.

$$\beta = -\frac{e}{\hbar}\oint_\gamma A_\mu dx^\mu + \frac{1}{\hbar}\oint_\gamma \mathbf{p}\cdot d\mathbf{x}. \tag{5.4}$$

where β is the AA's geometric phase, A_μ the electromagnetic four-potential, $\mathbf{p}$ the kinetic momentum, and γ the space-time closed curve of two electrons propagating through the two arms for the ring. Because of time reversal symmetry between the two paths, the time component is zero, $\oint_\gamma A_0 dx^0 = 0$. Further, $\oint_\gamma \mathbf{p}\cdot d\mathbf{x} = 0$ for a complete trip around the ring. Therefore, we have

$$\beta = \frac{e}{\hbar}\oint_\gamma \mathbf{A}\cdot d\mathbf{x} = \frac{e}{\hbar}\Phi_{\mathrm{B}}. \tag{5.5}$$

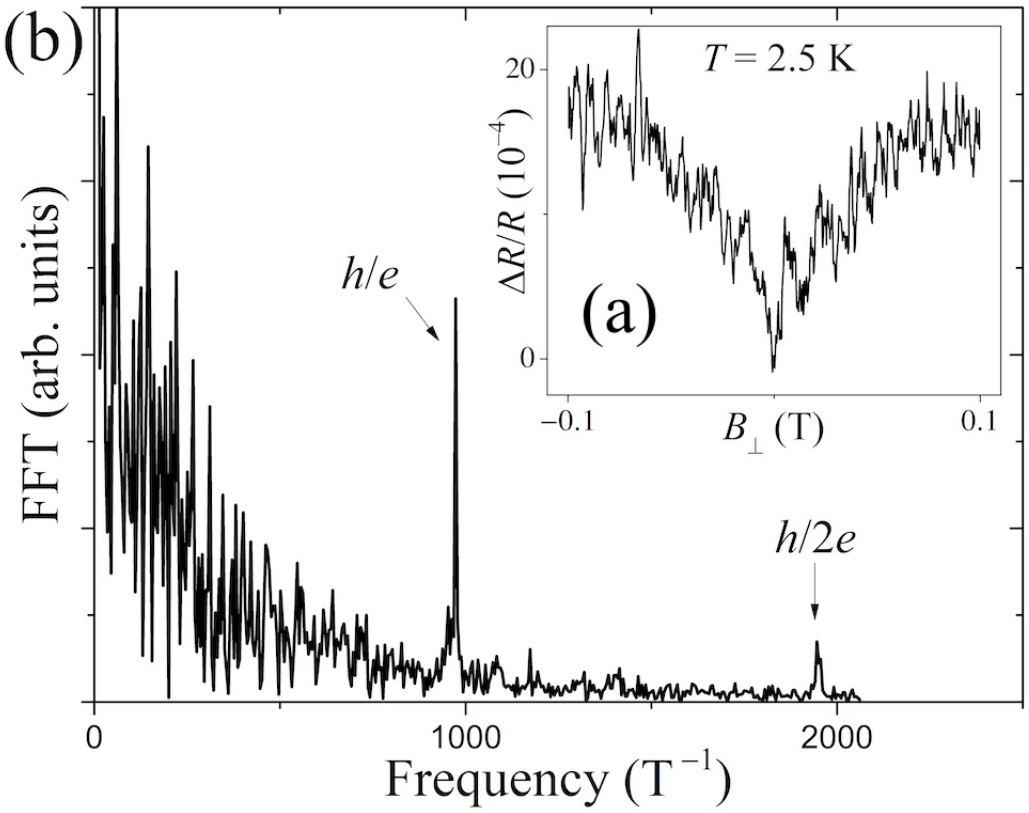

Figure 5.5 (a) Local Hanle effect (magnetoresistance) for a 2.2 μm ring with spin polarized current of 2 μA at 2.5 K. (b) FFT of the local Hanle curve for a 2.2 μm ring shows both h/e and $h/2e$ oscillations with peaks at 973 T^{-1} and 1948 T^{-1}.

where $\Phi_B = B_z \cdot S$ is the magnetic flux through the enclosed area of the ring.

With $B_\perp$ sweeping, a sinusoidal oscillation of non-local resistance with $\Delta B_z \cdot S = \frac{2\pi\hbar}{e}$ should be observed superimposed on the standard Hanle curve because precession does not break phase coherence. Figure 5.4a is a Hanle effect curve for the 0.95 μm ring with AC current of 0.5 μA at 1.9 K. By taking the Fourier transform of the Hanle curve, we observe a peak at 168 T^{-1} as in figure 5.4b. This peak corresponds to a resistance oscillation with period $\Delta B_z = 5.9$ mT. By calculating the average area of the hole enclosed by the ring, we get $\Delta B_z = 5.8$ mT. Considering that the accuracy of area measurement is 10%, this is very good agreement.

The difference in spin diffusion length between sample 2 and sample 1 is probably originated from pinholes on 2 nm thick MgO tunnel barrier. It is reported that in Graphene based non-local spin valve with MgO as tunnel barrier, the $\lambda_{sf} = 1.2$ μm for device with pinholes on tunnel barrier. For device with good tunneling, $\lambda_{sf} = 3.9$ μm (Wei Han et al., PRL, 105, 2010). We actually also observed similar effect for different groups of samples while fitting the Hanle curve. Practically in MgO sputtering, 2 nm thickness is very thin and difficult to be monitored accurately during deposition. In addition, considering the smoothness of thin film, it is very probably that pin holes exist on the MgO tunnel barrier.

5.4 Magnetoresistance with Spin Polarized Current

The local Hanle effect was observed by magnetoresistance measurements of a 2.2 μm diameter ring, showing an interference effect with spin polarized current and spin precession; both diffusive spin precession and drift current exist. A 2 μA AC current at 17 Hz was applied between Co1 and Co2 prepared parallel in plane and the voltage between NM1 and NM2 was measured via lock-in with $B_{\perp}$ sweeping. The magnetoresistance curve (Figure 5.5a) is weak-antilocalization-like [15], but fitting to the model [44] produces unreasonable results. This is understandable because Hikami's model does not consider spin polarization[44]. The Fourier transform of the magnetoresistance curve is shown in figure 5.5b. Two peaks at 973 T^{-1} and 1946 T^{-1} were clearly observed and, from equation 5.5 with $\beta = 2\pi$, correspond to h/e and $h/2e$ oscillations, respectively.

Chapter 6

Superconducting Spin Current

In order to study the spin transport properties in superconducting state Aluminum and the relevant interference effect with ring structure in the NLSV interferometer, the milliKelvin temperature measurement was performed for a Py/MgO/Al 1 diameter ring sample in dilution refrigerator. Only parallel magnetic field measurement was accomplished and presented here because the sample died while raising temperature and switching to a stage for perpendicular magnetic field measurement.

We observe that the spin signal does not depend markedly on temperature in the superconducting state, in contrast to what the quasiparticle picture suggests[82]. We also observe a localized increase in non-local resistance when both the detector and injector are in the negative parallel configuration and the temperature is below T_c (see figure 6.7).

Careful analysis and comparison with previous experimental and theoretical works suggest that, in the injection region, it is a Lateral Josephson Junction which can create the long range triplet components (LRTC) in the ferromagnetic injector [89, 12, 56]. The measured spin current in superconducting state Aluminum ring suggests that such LRTC with spin projection of ± 1 in FM1 can also leak into Aluminum, exist in Aluminum thin film for a short period of time, spread out in two directions at the injector region and finally detected by FM2, even though Aluminum is conventional superconductor and traditionally believed only spin-singlet Cooper pairs exist.

6.1 Introduction

It has been verified that spin triplet cooper pairs, once created, can diffuse in ferromagnet for a long distance while spin singlet cooper pair wave function declines rapidly in an oscillatory mode [13, 14]. In addition, theory also predicted different ways of spin singlet-triplet conversion in Ferromagnet/Superconductor hybrid structure [13, 12]: one is magnetic inhomogeneity near the S/F interface, such as non-collinear magnetization of magnetic multilayers [88] which has been experimentally realized widely (a typical work is from Robinson et al., [74]); another way to realize singlet-triplet conversion is to use spin-orbit (SO) coupling which can naturally generate long-range triplet components (LRTC) in ferromagnet [12]. In reference [12], a lateral Josephson junction as shown in figure 6.1 was also analyzed by Bergeret to explain the existing experimental result of 0 resistance of Cobalt nanowire with superconducting electrodes below T_c of the electrodes [12, 89].

6.2 Experimental Details

Py/MgO/Al NLSV interferometer samples group with ring diameter of 1 μm, 1.5 μm and 2 μm were fabricated as shown in figure 6.2. Often 12 samples were patterned on a single piece of Silicon wafer. First, FM1 and FM2 bars were patterned through E-beam lithography. The geometry of FM1 and FM2 are 12 μm$\times$1.5μm and 28 μm$\times$0.8μm. Different FM1/FM2 distances were designed to fit different diameter rings. After development, the samples were put into high vacuum chamber with base pressure of about 10^{-8} Torr for deposition. For this group of samples, magnetron sputtering was used for deposition. First, 20 nm of NiFe was deposited from $Ni_{80}Fe_{20}$ high purity target by DC magnetron sputtering. Then a 2 nm thick MgO layer was deposited from high purity MgO target by RF magnetron sputtering. After that, the sample was taken out for lift off in Aceton for about 1 hour. After rinse and

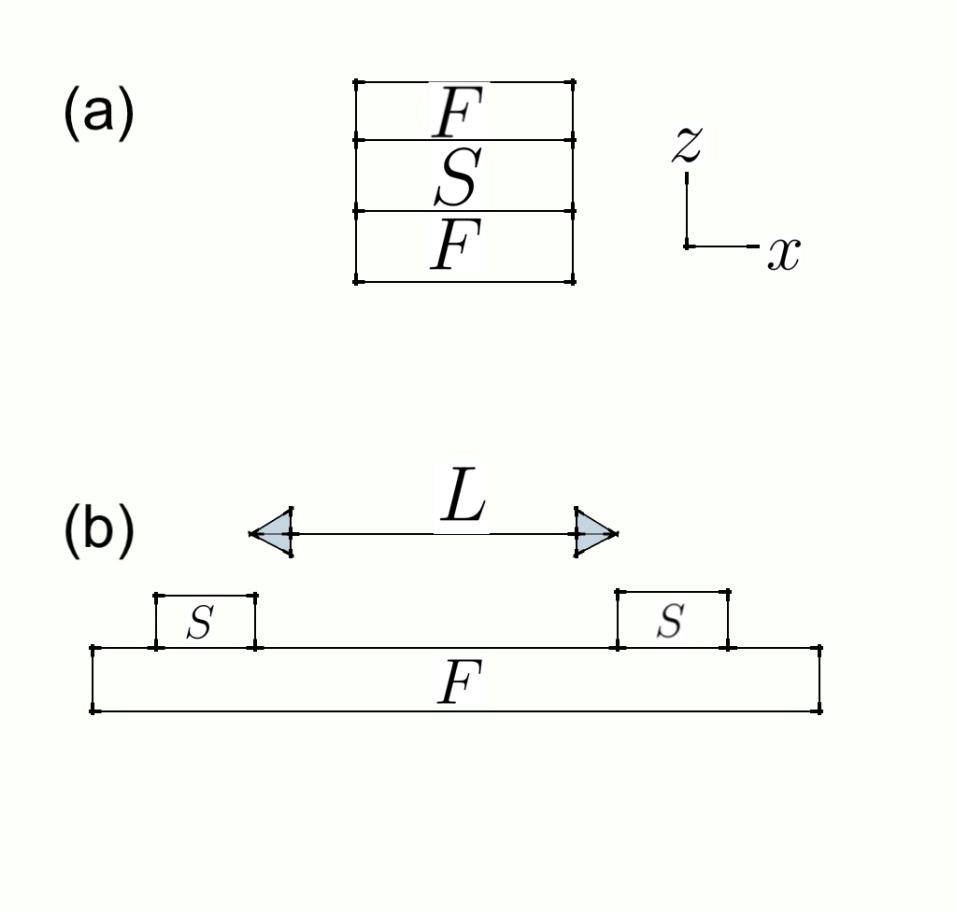

Figure 6.1 Different geometries of singlet-triplet conversion discussed theoretically by Bergeret [12]. b, lateral Josephson junction proposed by Bergeret for the explanation of 0 resistance of 600 nm long Co nanowire under T_c of Pb electrodes.[12, 89].

blow dry with Nitrogen gas, the sample was spin coated with double layer PMMA495 and PMMA950 followed by 90 seconds baking on 180°C hot plate thereafter. Then the second layer E-beam lithography was performed to pattern the rings for different samples. After development, the samples were cleaned with Argon ion to remove the possible contamination and developer. Then 60 nm thick Aluminum layer was DC sputtered. The typical ring samples are shown in figure 6.3 and figure 6.4. A bar sample as control was also fabricated at the same time in the same sample group as shown in figure 6.5

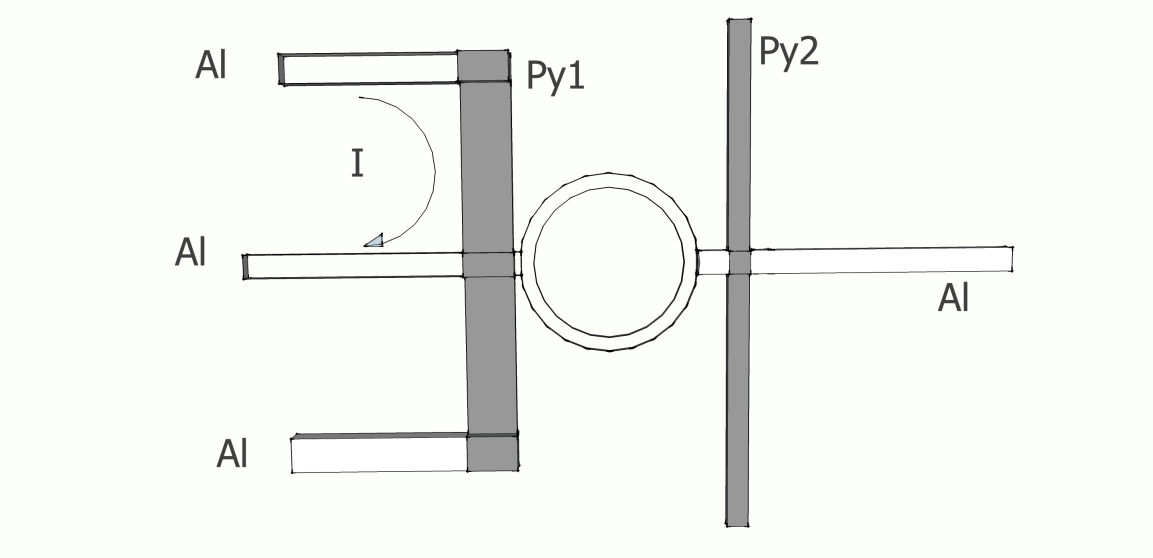

Figure 6.2 Schematic diagram of NLSV interferometer in our experiment. At the injection region, it is a lateral Josephson junction as Bergeret suggested in [12].

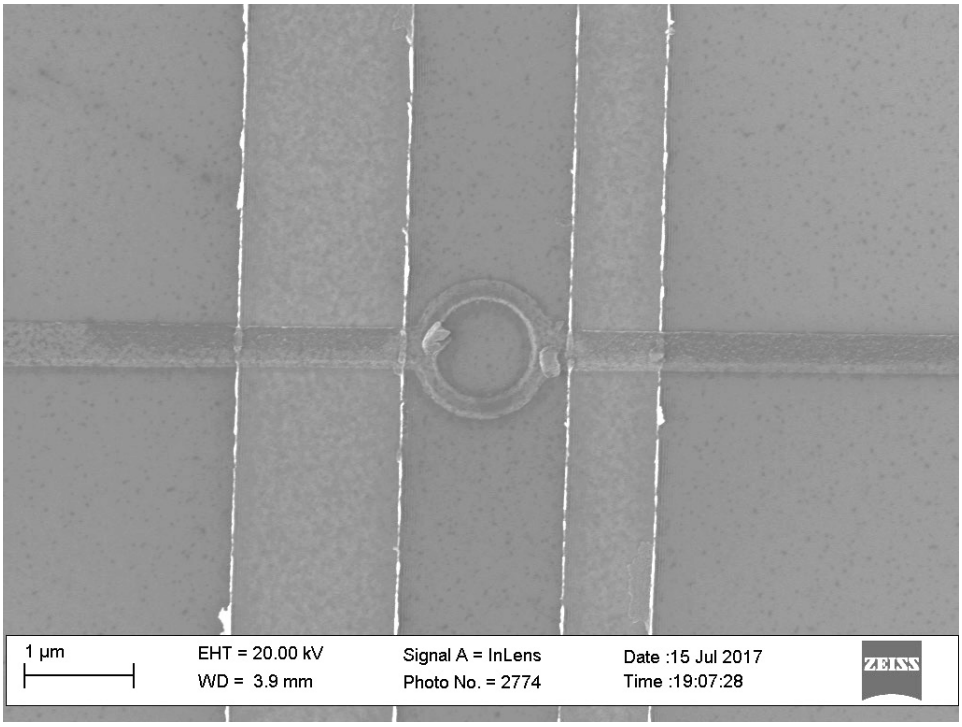

Figure 6.3 SEM image of a typical 1 μm diameter ring Py/MgO/Al NLSV interferometer ring sample.

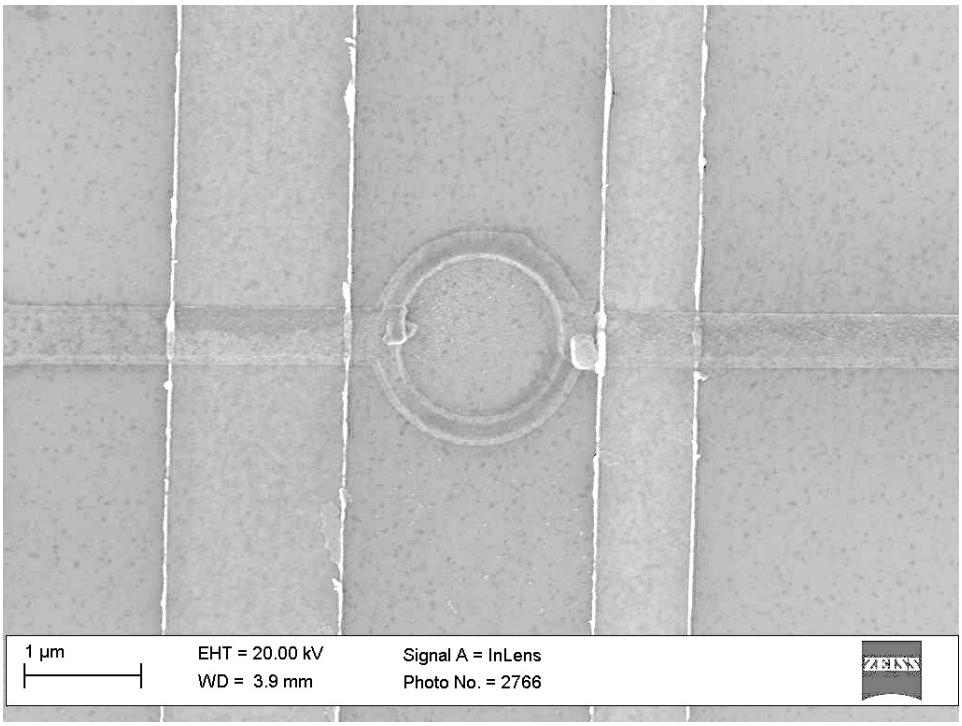

Figure 6.4 SEM image of a typical 1.5 μm diameter ring Py/MgO/Al NLSV interferometer ring sample.

Previous works[73, 67] on NLSV bar systems have shown a marked change in ΔR_{NL} as the temperature crosses T_c from above, therefore, we made non-local spin measurements at a range of temperatures from 50 milliKelvin to 1.6 K, above T_c. A Py/MgO|Al 1 μm diameter ring sample was cooled to 50 mK in a dilution refrigerator. Non-local resistance was measured with an AC injection currents of 0.125 μA, 0.25 μA, 0.5 μA, 1 μA and 2 μA at 79 Hz[33]. Before measurement, a +1 T high magnetic field was once applied parallel to FM1 and FM2. Magnetic field was then swept between -0.03 T and $+0.03$ T parallel to the injector and detector in plane at different temperature at the rate of 10 Gauss per minute. To measure the T_C, a quasi-static temperature sweep was performed at the rate of 1 mK per minute with injection current of 0.5 μA, 1 μA and 2μA respectively . To find out Critical field at different temperature, parallel magnetic field was swept between -700 G +700 G at 60 Gauss

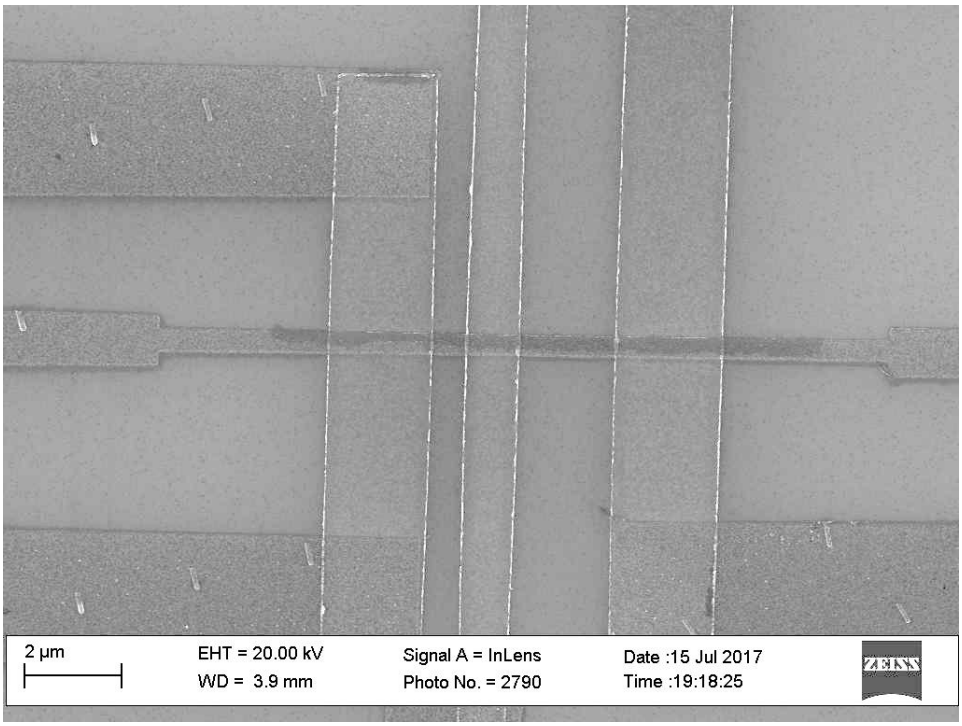

Figure 6.5 SEM image of a Py/MgO/Al NLSV bar sample serving as control.

per minute at 1.4 K, −1000 G and +1000 G at 60 Gauss per minute at 1.3 K.

6.3 Results and Discussion

6.3.1 Inconsistency with Prediction from Bogoliubov Quasiparticle Theory

The inset of figure 6.6 shows T_c detection with 3 different FM configuration with Injection current of 0.5 μA. We find $T_c = 1.54$ K with the non-local resistance baseline jumping from 127.6 Ω to 122 Ω. T_c shift of 5 mK, which is due to spin polarization difference[66], was observed only with opposite magnetization direction of injector. Spin current is clearly seen below, above, and at T_c in figure 6.6. The critical field at $T = 1.5$ K was found to be $B_{c,\|} = 0.025$ T.

To compare the spin resistance, we offset the 1.6 K data as in figure 6.7. ΔR_{NL} in the superconducting state is almost identical to that in the normal state. However,

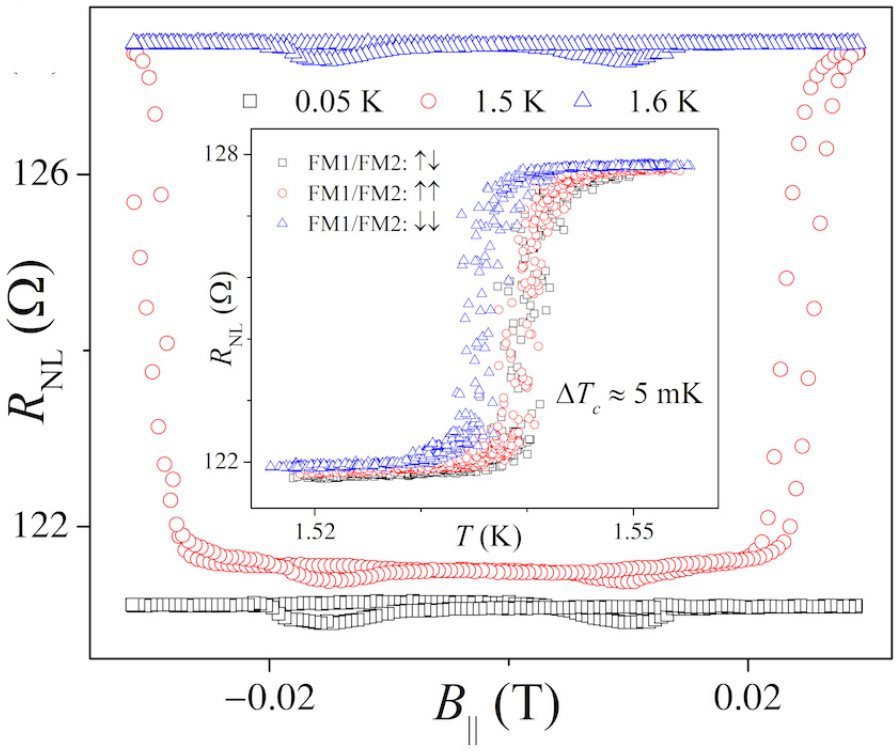

Figure 6.6 Co-existence of spin current and superconductivity. Non-local resistance curve with $B_{\|}$ swept between ±0.03 T at the normal state (1.6 K), superconducting state (0.05 K), and at 1.5 K with a critical field of $B_c = 0.025$ T. Inset: T_c shift for different injector and detector configurations with quasi-static change of temperature at $B_{\|} = 0$. The superconducting transition temperature depends on the degree of spin polarization[66]. If this is controlled primarily by the injector, we would expect T_c for the the ↑↓ and ↑↑ states to be equal but different than for the ↓↓ state, consistent with our observations.

below T_c, as the field approaches the point when either FM1 and FM2 are in the negative parallel configuration, the non-local resistance increases (arrows in figure 6.7). The magnitude of the increase grows as the temperature approaches T_c from below and vanishes above T_c. This effect may come from the interaction between Cooper pairs and magnetic domains[62, 61].

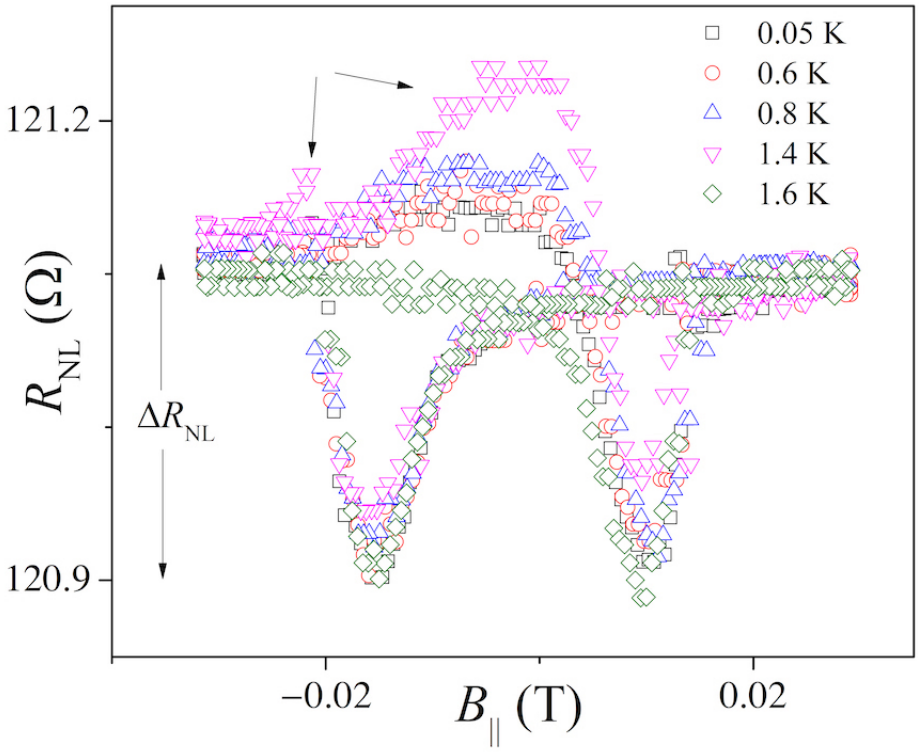

Figure 6.7 Co-existence of spin current and superconductivity. Non-local resistance at various temperatures below and above T_c and at at 1.6 K, after removing the offset due to the superconducting transition. ΔR_{NL} does not change with temperature either below or above T_c, which is inconsistent with the theoretical predictions of several orders of magnitude change below T_c based on the quasiparticle picture. In addition, arrows point out a localized increase of R_{NL} below T_c when FM1 and FM2 are in the negative parallel configuration. The effect increases as the temperature approaches T_c from below and disappears after the transition. Every 10^{th} data point shown for clarity.

The almost identical spin resistance below and above T_c is inconsistent with theoretical predictions based on the quasiparticle picture[82] which suggest a temperature dependent enhancement of spin resistance by the factor of $1/2f_0(\Delta)$ at the superconducting state, where Δ is the superconducting gap and f_0 is the Fermi distribution function[82, 73, 11]. The spin signal in superconducting state was calculated as [82]

$$R_s = V_s/I = \frac{1}{2f_0(\Delta)} P_J^2 R_N e^{-L/\lambda_N} \tag{6.1}$$

The magnitude of the enhancement was predicted to be several orders of magnitude above the normal state[82, 73, 11].

6.3.2 Non-local Spin Signal Baseline Jump as Evidence of Superconductivity

Experimentally in quasi-one-dimensional metal wire the baseline of non-local resistance always exists. One of the origins of the baseline is non-uniform spin injection at FM/I/N interface due to the non-uniform thickness of tunnel barrier or pinholes(leakage current) [54]. Such a non-uniform spin injection leads to an electric field between injector and detector[54]. Therefore, for non-local resistance measurement as in figure 6.6 in the manuscript, electric field also exists between injector and detector to generate drift current which contributes to non-local voltage baseline. Below T_c, drift current becomes supercurrent, the corresponding voltage contribution to baseline also jumps to 0. (This is also a signature of existence of drift current in non-local measurement to referee's issue 4). According to BCS theory, in superconducting state, all the electrons should behave as a whole. Therefore the jump of baseline can be used as evidence for superconductivity of the Al nano-ring. The jump of baseline also appears on critical field B_c.

Several factors can convert superconducting Al ring to normal state in authors' device under vacuum down to 50 mK: 1, current density (j) larger than critical current

density(j_c); 2, Temperature T higher than critical temperature T_c; 3, Magnetic field B larger than critical field B_c.

1, In our experiment, we used current of 0.125 μA, 0.25μA, 0.5 μA, 1 μA and 2 μA. For this Py/MgO/Al sample, the cross sectional area at the injector is about 0.5 μm^2. The current density across the junction is 4 μA/μm^2. The thickness of Al is 0.06 μm, width is 0.3 μm, the current density through the NM1 wire is to the order of 100 μA/μm^2. For Al nanowire thin film, the critical current density was reported to be to the order of 10^{11} A/m^2 = 10^5 μA/μm^2 near $T = 0$ K [75]. Therefore, considering the Ginsberg-Landau result,

$$j_c = j_c(0)(1 - \frac{T}{T_c})^{3/2}, \tag{6.2}$$

the current density in our experiment is 2-3 orders of magnitude smaller than the critical current density of Al.

2, The critical temperature was carefully examined in the inset of figure 6.6. For our 60 nm thick Al thin film, $T_c = 1.54$ K is well consistent with previous report [80].

3, The critical field was also examined at 1.5 K, 1.4 K and 1.3 K as shown in figure 6.8.

In addition, there is one tiny possibility that Aluminum film is normal metal under T_c. That is to deposit Al film with water cooled substrate through e-gun evaporation under the 100 mT oxygen pressure such that the AlO_x concentration is high and lead to superconductor-normal metal-insulator conversion [58]. In our manuscript, the sample in figure 6.6 is prepared by magnetron sputtering in high vacuum chamber (base pressure $10^{(-8)}$ Torr). Aluminum layer is DC sputtered with working gas of high purity Argon. It is unreasonable to assume such high AlO_x concentration that makes Al normal metal below T_c. Even if one argues that there might be very tiny possibility that Al film is normal metal below T_c, our answer is because of the voltage jump in figure 6.6, something must be superconducting, but we have not find out any

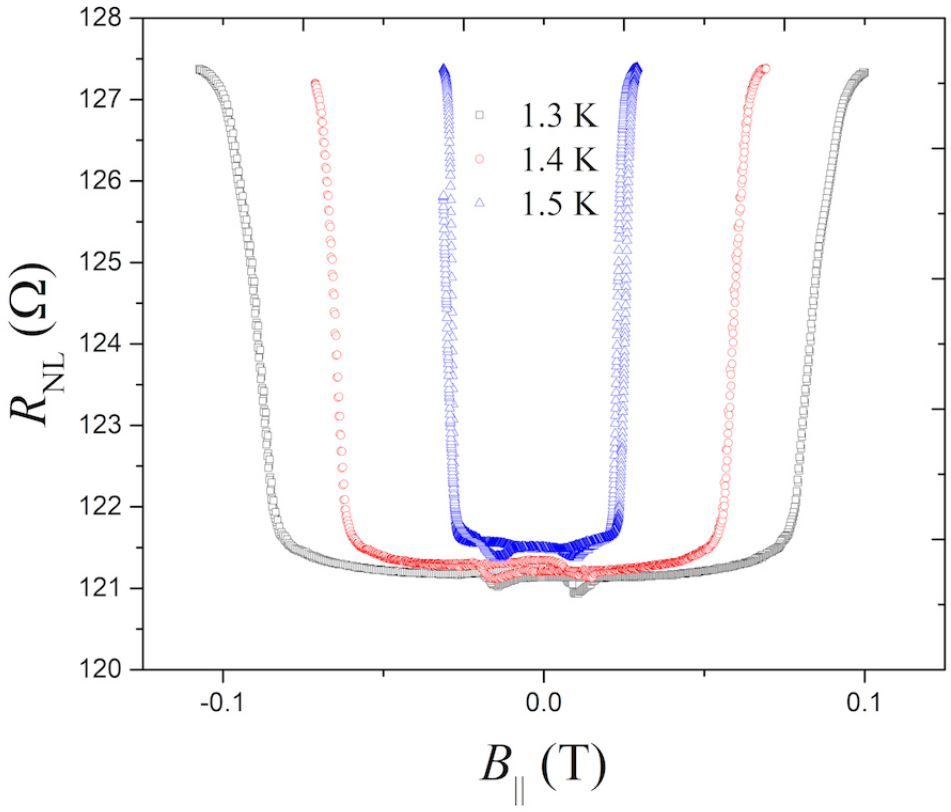

Figure 6.8 Critical field at different temperature.

literature that reports Py wire can be superconducting with normal metal electrodes at 1.5 K.

Spin polarization in Al thin film can shift the T_c from 2.58 K to 2.13 K [66], below 2.13 K in their work, Al film is always superconducting. In our manuscript, we also observed T_c shift because of different spin polarization. But spin polarization in Al film can not convert Al from superconductor to normal metal down to 50 mK.

Based on the above analysis, we conclude the Al nano-ring is superconducting.

6.3.3 Superconducting Spin Signal with Different Injection Current

Non-local spin signal with different injection currents (1 μA, 0.5 μA) was also measured. Similar baseline jumping was found when temperature was below T_C as shown in figure 6.9 and figure 6.10. Spin resistances were almost the same with different injection current, either above or below T_C. At 1.5 K, the critical field is higher for smaller injection current, which further prove the baseline jump is due to superconducting transition.

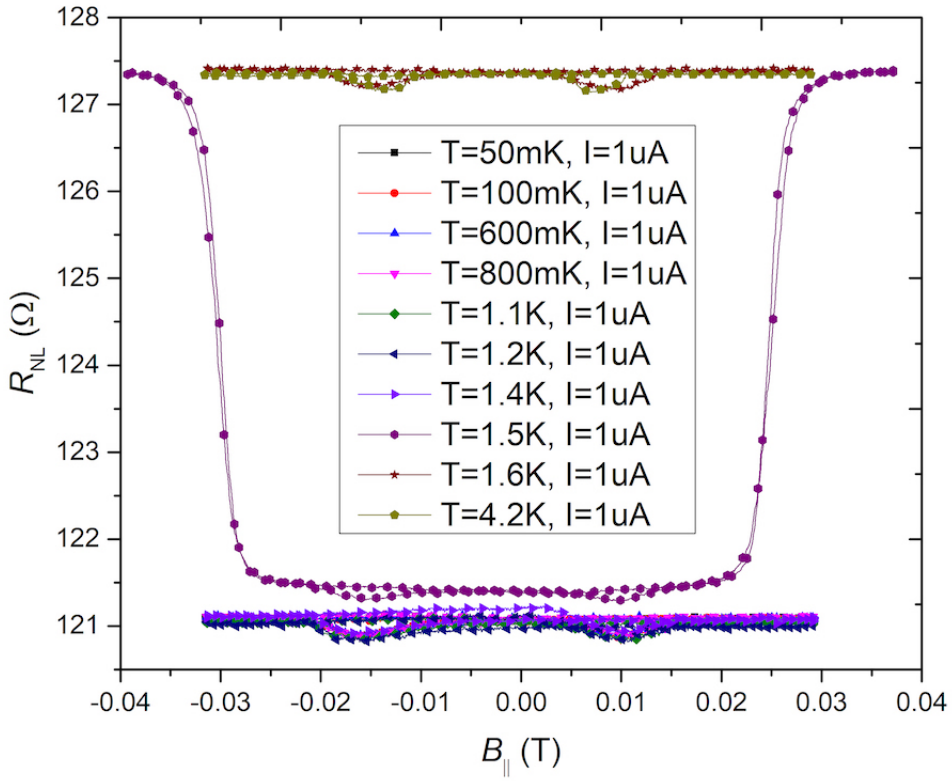

Figure 6.9 Non-local resistance with injection current of 1 μA at temperature from 50 mK to 4.2 K.

The clear non-local resistance comparison for 0.5 μA, 1 μA and 2 are shown in figure 6.11, figure 6.12 and figure 6.13. For 2 μA, The asymmetry of non-local

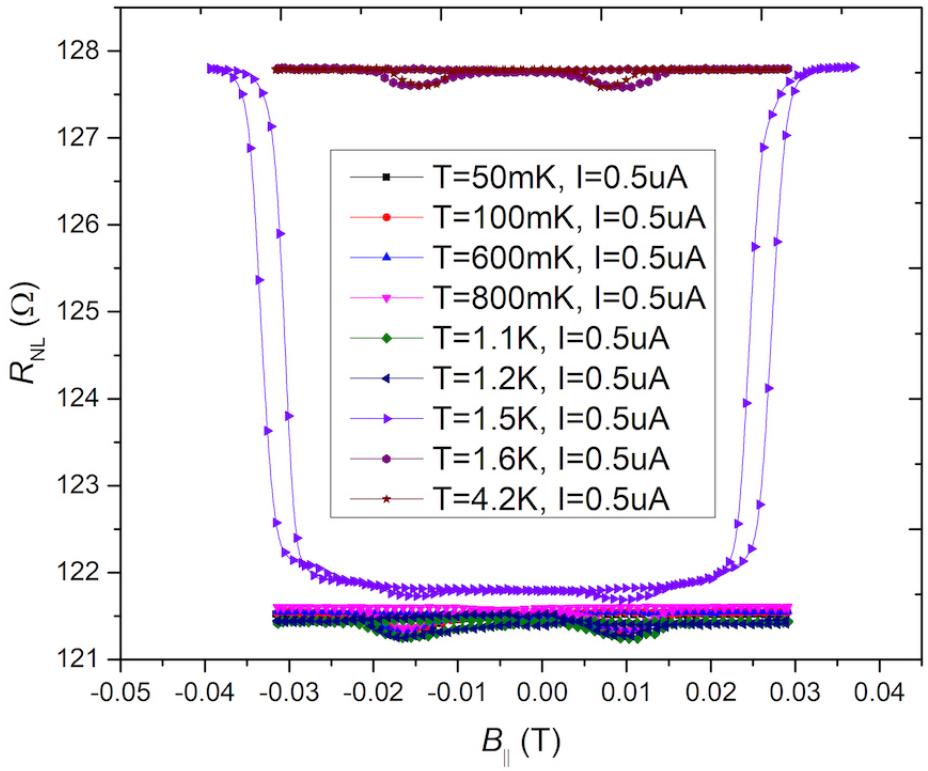

Figure 6.10 Non-local resistance with injection current of 0.5 μA at temperature from 50 mK to 4.2 K.

resistance for positive and negative field sweep exist at all temperature from 50 mK to 1.4 K below T_C. Such asymmetry increases gradually with temperature. However, for 1 μA injection current, the non-local resistance shows a dramatic change below and above 1.1 K. From 50 mK to 800 mK for 1 μA injection current, the non-local resistances are almost at the same level with similar profile but a slight increase with rising temperature. Above 1.1 K, the shape of non-local resistances change a lot with baseline first drop at 1.1 K then increase at 1.2 K and 1.4 K.

Such phenomena is more obvious for the 0.5 μA low temperature data with another feature, that is the asymmetry of non-local resistances for positive and negative field scan totally disappears between 50 mK to 800 mK. Such asymmetry only exist above

1.1 K. Please note that there is an equipment field offset for the 0 magnetic field.

Such phenomena suggest that the state of Aluminum spacer below 800 mK and above 1.1 K are different even though it is still in superconducting state. The relevant spin transport behavior is also different. The physics origin is not clear. For bulk aluminum, the critical temperature is about 1.17 K. For aluminum thin film in which electrons are confined in two dimensions, T_C is higher than that in bulk aluminum. We suggest, maybe there is a phase change at temperature T_{C1} around 1.1 K in aluminum thin film, such that below T_{C1}, spin singlet correlation dominates, while above T_{C1}, spin triplet correlation also exists. Such supposition needs more theoretical and experimental work to confirm.

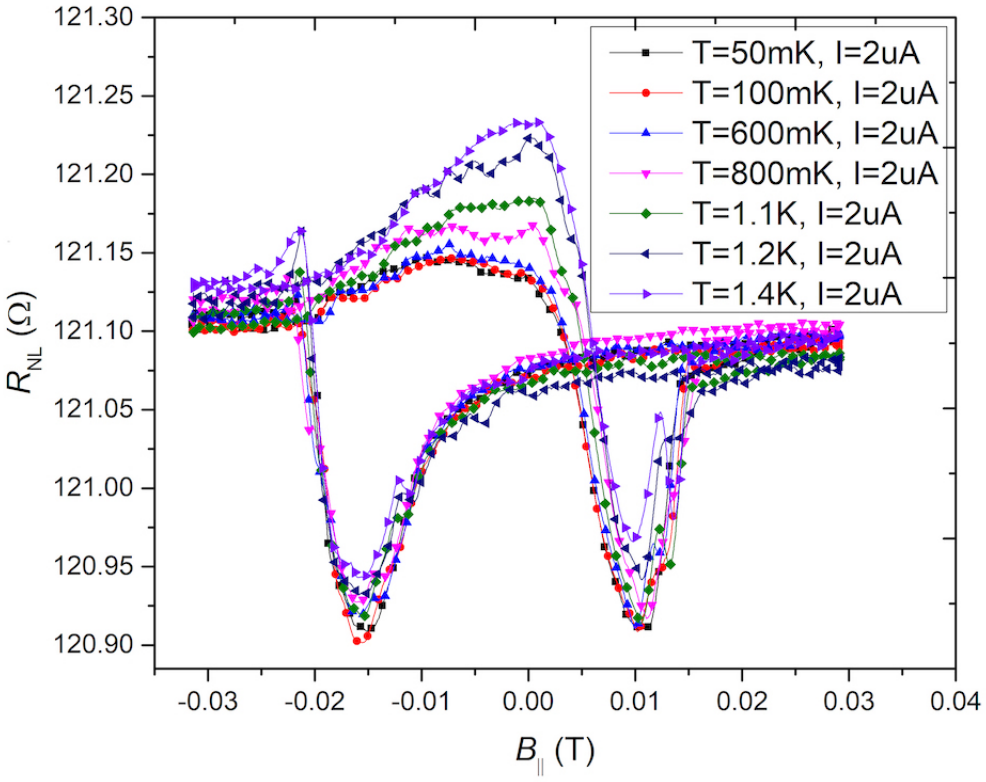

Figure 6.11 Non-local resistance with injection current of 2 μA at various temperature below T_C.

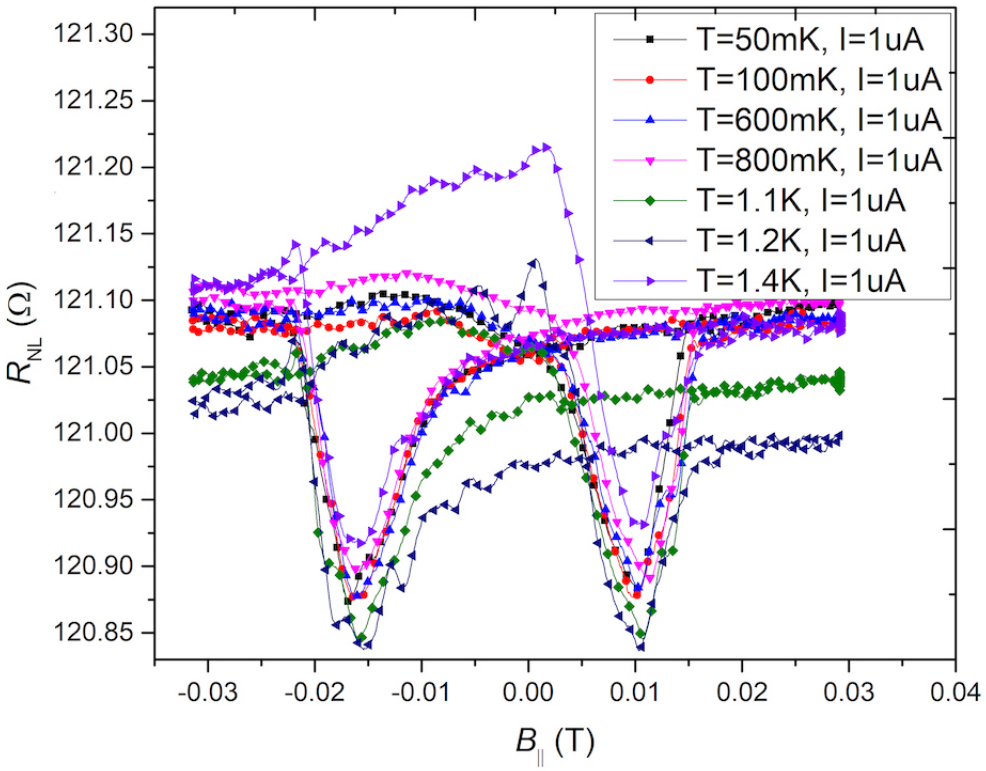

Figure 6.12 Non-local resistance with injection current of 1 μA at various temperature below T_C.

The co-existence of superconductivity and spin current in our device could be direct evidence of spin supercurrents from spin triplet Cooper pairs, which were under experimental and theoretical investigation recently[62]. In our work, below T_c, in the injection region, it is actually a lateral Josephson junction [12] with Al/I/FM1/I/Al structure with FM1 length of $< 4\mu$m. Therefore, across the first junction, the the long range triplet components with spin projection ± 1 are generated in FM1 due to SO coupling [12]. In FM1, the long range triplet components propagate to the cross-section on the left of the ring and penetrate into Aluminum.

Because we continue to observe spin current in the superconducting state, we suggest that, similar to superfluid ^{3}He, the spin triplet states $|\uparrow\uparrow\rangle$, $|\downarrow\downarrow\rangle$ and $\frac{1}{\sqrt{2}}(|\uparrow\downarrow\rangle +$

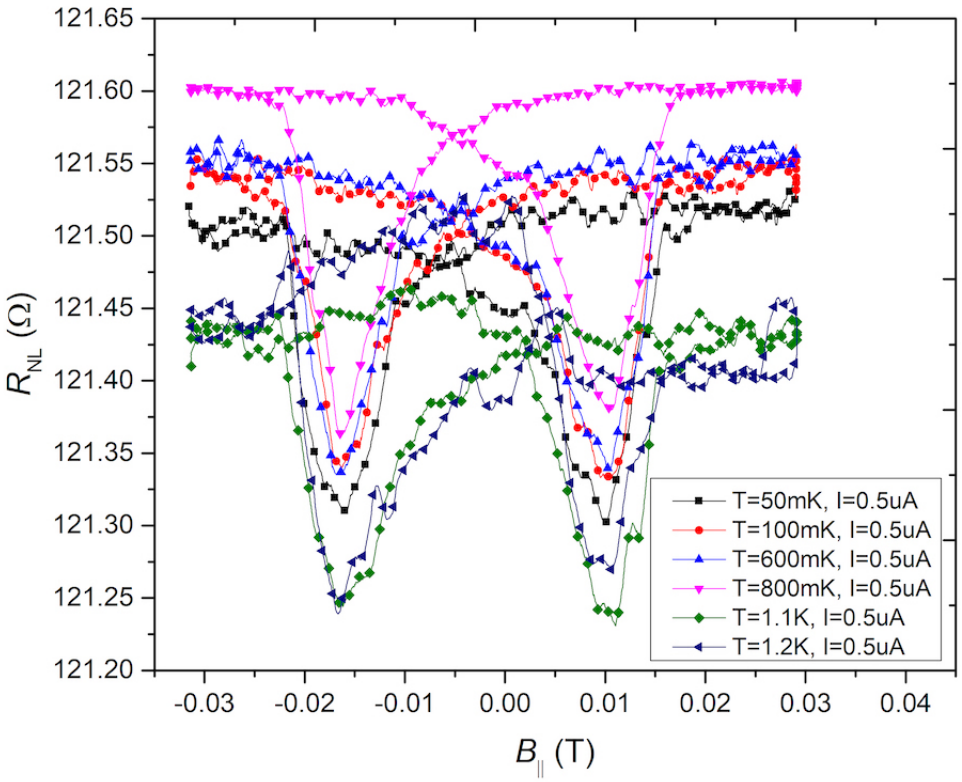

Figure 6.13 Non-local resistance with injection current of 0.5 μA at various temperature below T_C.

$|\downarrow\uparrow\rangle$), among which $|\uparrow\uparrow\rangle$ and $|\downarrow\downarrow\rangle$ have non-zero spin and therefore can also cause a spin current, may also exist in thin films of Al with direct spin injection from a FM, even though Al is traditionally categorized as a type I superconductor in which only spin singlet Cooper pairs exist[92, 10, 77]. Al is type one superconductor, such spin-triplet states $|\uparrow\uparrow\rangle$, $|\downarrow\downarrow\rangle$ are not stable, therefore, they decline in two directions at the injector region and detected by the detector FM2 in the nonlocal spin signal. Consistent with this supposition, recent experimental work on spin pumping into superconductors has shown evidence of triplet spin supercurrent and not quasiparticles[52]. For a clear understanding of the spin triplet components transport and relaxation behavior in type I, more theoretical and experimental work is needed.

Chapter 7

Conclusion

To conclude, we experimentally observed simultaneous h/e oscillation and Hanle spin precession in the NLSV interferometer above T_c for an Al ring spacer. Because the non-adiabatic condition is satisfied at low fields when the time for an electron to transit the ring is shorter than the period of Larmor precession, our measurement is an experimental observation of AA's non-adiabatic geometric phase and not an AB phase measurement. In addition, we observed the co-existence of spin current and superconductivity. The identical spin resistance above and below T_c is inconsistent with predictions from quasiparticle theories.With consideration of Lateral Josephson Junction at the injection region, long range triplet components with spin projection of ± 1 formed in the short Py injector. Such long range triplet components in Py could propagate to the injector junction and spread into Al. Since Al is conventional superconductor, the triplet components might not be stable and may decay in two directions. As a result, we suggest the superconducting spin current may come from spin triplet Cooper pairs.

Bibliography

[1] A.A. Abrikosov and L.P. Gor'kov, *Spin-orbit interaction and the knight shift in superconductors*, Sov. Phys. JETP **15** (1962), 752.

[2] Y. Aharonov and J. Anandan, *Phase change during a cyclic quantum evolution*, Physical Review Letters **58** (1987), no. 16, 1593–1596.

[3] Y. Aharonov and D. Bohm, *Significance of electromagnetic potentials in the quantum theory*, Physical Review **115** (1959), 485.

[4] Johan Åkerman, *Toward a universal memory*, Science **308** (2005), no. 5721, 508–510.

[5] B. L. Altshuler, A. G. Aronov, and B. Z. Spivak, *The aharonov-bohm effect in disordered conductors*, Pis'ma Zh. Eksp. Teor. Fiz. **33** (1981), 101–103.

[6] B. L. Altshuler, A. G. Aronov, B. Z. Spivak, D. Yu. Sharvin, and Yu. V. Sharvin, *Observation of the aharonov-bohm effect in hollow metal cylinders*, Pis'ma Zh. Eksp. Teor. Fiz. **35** (1982), 476–478.

[7] Jeeva Anandan, *The geometric phase*, Nature **360** (1992), no. 6402, 307–313.

[8] N. W. Ashcroft and N. D. Mermin, *Solid state physics*, Cengage Learning, 1976.

[9] M. N. Baibich, *Giant magnetoresistance of (001)fe/(001)cr magnetic superlattices*, Physical Review Letters **61** (1988), no. 21, 2472–2475.

[10] A. V. Balatsky, I. Vekhter, and Jian-Xin Zhu, *Impurity-induced states in conventional and unconventional superconductors*, Reviews of Modern Physics **78** (2006), no. 2, 373–433.

[11] D. Beckmann, *Spin manipulation in nanoscale superconductors*, Journal of Physics: Condensed Matter **28** (2016), no. 16, 163001.

[12] F. S. Bergeret and I. V. Tokatly, *Singlet-triplet conversion and the long-range proximity effect in superconductor-ferromagnet structures with generic spin dependent fields*, Physical Review Letters **110** (2013), no. 11, 117003.

[13] F. S. Bergeret, A. F. Volkov, and K. B. Efetov, *Long-range proximity effects in superconductor-ferromagnet structures*, Physical Review Letters **86** (2001), no. 18, 4096–4099.

[14] F. S. Bergeret, A. F. Volkov, and K. B. Efetov, *Odd triplet superconductivity and related phenomena in superconductor-ferromagnet structures*, Reviews of Modern Physics **77** (2005), no. 4, 1321–1373.

[15] Gerd Bergmann, *Weak localization in thin films: a time-of-flight experiment with conduction electrons*, Physics Reports **107** (1984), 1–58.

[16] M. V. Berry, *Quantal phase factors accompanying adiabatic changes*, Proceedings of the Royal Society A: Mathematical, Physical and Engineering Sciences **392** (1984), no. 1802, 45–57.

[17] M. V. Berry, *Quantum phase corrections from adiabatic iteration*, Proceedings of the Royal Society A: Mathematical, Physical and Engineering Sciences **414** (1987), no. 1846, 31–46.

[18] G. L. Bir and G. E. Pikus A. G. Aronov, *Spin relaxation of electrons due to scattering by holes*, Sov. Phys. JETP **42** (1976), 705–712.

[19] T. Bitter and D. Dubbers, *Manifestation of berry's topological phase in neutron spin rotation*, Physical Review Letters **59** (1987), no. 3, 251–254.

[20] M. Born and V. Fock, *Beweis des adiabatensatzes*, Zeitschrift fur Physik **51** (1928), no. 3-4, 165–180.

[21] M. Bowen, V. Cros, F. Petroff, A. Fert, C. Martinez Boubeta, J. L. Costa-Krämer, J. V. Anguita, A. Cebollada, F. Briones, J. M. de Teresa, and et al., *Large magnetoresistance in fe/mgo/feco(001) epitaxial tunnel junctions on gaas(001)*, Applied Physics Letters **79** (2001), no. 11, 1655–1657.

[22] R. G. Chambers, *Shift of an electron interference pattern by enclosed magnetic flux*, Physical Review Letters **5** (1960), no. 1, 3–5.

[23] V. Chandrasekhar, M. J. Rooks, S. Wind, and D. E. Prober, *Observation of aharonov-bohm electron interference effects with periods h/e and h/2e in individ-*

ual micron-size, normal-metal rings, Physical Review Letters **55** (1985), no. 15, 1610–1613.

[24] Claude Chappert, Albert Fert, and Frédéric Nguyen Van Dau, *The emergence of spin electronics in data storage*, Nature Materials **6** (2007), no. 11, 813–823.

[25] Raymond Y. Chiao and Yong-Shi Wu, *Manifestations of berry's topological phase for the photon*, Physical Review Letters **57** (1986), no. 8, 933–936.

[26] Saroj P. Dash, Sandeep Sharma, Ram S. Patel, Michel P. de Jong, and Ron Jansen, *Electrical creation of spin polarization in silicon at room temperature*, Nature **462** (2009), no. 7272, 491–494.

[27] S. Datta, *Novel interference effects between parallel quantum wells*, Physical Review Letters **55** (1985), no. 21, 2344–2347.

[28] M. I. Dyakonov and V. I. Perel, *Spin relaxation of conduction electrons in noncentrosymmetric semiconductors*, Sov. Phys. Solid State **13** (1972), no. 12, 3023–3026.

[29] M. I. D'yakonov and V. I. Perel, *Optical orientation in a system of electrons and lattice nuclei in semiconductors theory*, Sov. Phys. JETP **38** (1973), 177–183.

[30] R. J. Elliott, *Theory of the effect of spin-orbit coupling on magnetic resonance in some semiconductors*, Physical Review **96** (1954), no. 2, 266–279.

[31] Albert Fert, *Nobel lecture: Origin, development, and future of spintronics*, Reviews of Modern Physics **80** (2008), no. 4, 1517–1530.

[32] D. Frustaglia, M. Hentschel, and K. Richter, *Quantum transport in nonuniform magnetic fields: Aharonov-bohm ring as a spin switch*, Physical Review Letters **87** (2001), no. 25, 256602.

[33] Yasuhiro Fukuma, Le Wang, Hiroshi Idzuchi, Saburo Takahashi, Sadamichi Maekawa, and YoshiChika Otani, *Giant enhancement of spin accumulation and long-distance spin precession in metallic lateral spin valves*, Nature Materials **10** (2011), no. 7, 527–531.

[34] X. C. Gao and T. Z. Qian, *Aharonov-anandan phase and persistent currents in a mesoscopic ring*, Physical Review B **47** (1993), no. 12, 7128–7131.

[35] John C. Garrison and Raymond Y. Chiao, *Geometrical phases from global gauge invariance of nonlinear classical field theories*, Physical Review Letters **60** (1988), no. 3, 165–168.

[36] Samir Garzon, Igor Žutić, and Richard A. Webb, *Temperature-dependent asymmetry of the nonlocal spin-injection resistance: Evidence for spin nonconserving interface scattering*, Physical Review Letters **94** (2005), no. 17, 176601.

[37] J. Hamrle, T. Kimura, Y. Otani, K. Tsukagoshi, and Y. Aoyagi, *Current distribution inside py/cu lateral spin-valve devices*, Physical Review B **71** (2005), no. 9, 094402.

[38] W. Han, K. M. McCreary K. Pi, Y. Li, Jared J. I. Wong, A. G. Swartz, and R. K. Kawakami, *Tunneling spin injection into single layer graphene*, Physical Review Letters **105** (2010), 167202.

[39] W Han, R. K. Kawakami, M. Gmitra, and J. Fabian, *Graphene spintronics*, Nature Nanotechnology **9** (2014), no. 10, 794–807.

[40] J H Hannay, *Angle variable holonomy in adiabatic excursion of an integrable hamiltonian*, Journal of Physics A: Mathematical and General **18** (1985), no. 2, 221–230.

[41] C. Harmans, *Mesoscopic physics: An introduction*, TU Delft, 2003.

[42] H. Heinrich, G. Bauer, and eds. F. Kuchar, *Physics and technology of submicron structures*, Springer, Berlin, 1988.

[43] M. Hentschel, H. Schomerus, D. Frustaglia, and K. Richter, *Aharonov-bohm physics with spin. i. geometric phases in one-dimensional ballistic rings*, Physical Review B **69** (2004), no. 15, 155326.

[44] S. Hikami, A. I. Larkin, and Y. Nagaoka, *Spin-orbit interaction and magnetoresistance in the two dimensional random system*, Progress of Theoretical Physics **63** (1980), 707.

[45] H. Idzuchi, Y. Fukuma, L. Wang, and Y. Otani, *Spin relaxation mechanism in silver nanowires covered with mgo protection layer*, Applied Physics Letters **101** (2012), no. 2, 022415.

[46] Hiroshi Idzuchi, Yasuhiro Fukuma, and YoshiChika Otani, *Spin transport in non-magnetic nano-structures induced by non-local spin injection*, Physica E: Low-dimensional Systems and Nanostructures **68** (2015), 239 – 263.

[47] Thomas Ihn, *Oscillations in the ribbons*, Nature Materials **9** (2010), no. 3, 187–188.

[48] S. Ikeda, J. Hayakawa, Y. Ashizawa, Y. M. Lee, K. Miura, H. Hasegawa, M. Tsunoda, F. Matsukura, and H. Ohno, *Tunnel magnetoresistance of 604at 300k by suppression of ta diffusion in cofeb/mgo/cofeb pseudo-spin-valves annealed at high temperature*, Applied Physics Letters **93** (2008), no. 8, 082508.

[49] F. J. Jedema, A. T. Filip, and B. J. van Wees, *Electrical spin injection and accumulation at room temperature in an all-metal mesoscopic spin valve*, Nature **410** (2001), no. 6826, 345–348.

[50] F. J. Jedema, H. B. Heersche, A. T. Filip, J. J. A. Baselmans, and B. J. van Wees, *Electrical detection of spin precession in a metallic mesoscopic spin valve*, Nature **416** (2002), no. 6882, 713–716.

[51] F. J. Jedema, M. S. Nijboer, A. T. Filip, and B. J. van Wees, *Spin injection and spin accumulation in all-metal mesoscopic spin valves*, Physical Review B **67** (2003), no. 8, 085319.

[52] K.-R. Jeon, C. Ciccarelli, A. J. Ferguson, H. Kurebayashi, L. F. Cohen, X. Montiel, M. Eschrig, J. W. A. Robinson, and M. G. Blamire, *Enhanced spin pumping into superconductors provides evidence for superconducting pure spin currents*, Nature Materials **17** (2018), 499–503.

[53] Mark Johnson, *Interfacial charge-spin coupling: Injection and detection of spin magnetization in metals*, Physical Review Letters **55** (1985), no. 17, 1790–1793.

[54] Mark Johnson, *Calculation of nonlocal baseline resistance in a quasi-one-dimensional wire*, Physical Review B **76** (2007), no. 15, 153107.

[55] M. Julliere, *Tunneling between ferromagnetic films*, Physics Letters A **54** (1975), no. 3, 225 – 226.

[56] R. S. Keizer, S. T. B. Goennenwein, T. M. Klapwijk, G. Miao, G. Xiao, and A. Gupta, *A spin triplet supercurrent through the half-metallic ferromagnet cro2*, Nature **439** (2006), no. 7078, 825–827.

[57] T. Kimura and Y. Otani, *Large spin accumulation in a permalloy-silver lateral spin valve*, Physical Review Letters **99** (2007), no. 19, 196604.

[58] M. Kunchur, P. Lindenfeld, W. L. McLean, and J. S. Brooks, *Absence of superconductivity in metallic granular aluminum*, Physical Review Letters **59** (1987), no. 11, 1232–1235.

[59] R. Landauer, *Spatial variation of currents and fields due to localized scatters in metallic conduction*, IBM Journal of Research and Development **1** (1957), 223–231.

[60] A. I. Larkin, *Reluctance of two-dimensional systems*, JETP Lett **31** (1980), 219.

[61] Jacob Linder and Klaus Halterman, *Superconducting spintronics with magnetic domain walls*, Physical Review B **90** (2014), 104502.

[62] Jacob Linder and Jason W. A. Robinson, *Superconducting spintronics*, Nature Physics **11** (2015), no. 4, 307–315.

[63] Daniel Loss, Paul Goldbart, and A. V. Balatsky, *Berry's phase and persistent charge and spin currents in textured mesoscopic rings*, Physical Review Letters **65** (1990), no. 13, 1655–1658.

[64] Xiaohua Lou, Christoph Adelmann, Scott A. Crooker, Eric S. Garlid, Jianjie Zhang, K. S. Madhukar Reddy, Soren D. Flexner, Chris J. Palmstrøm, and Paul A. Crowell, *Electrical detection of spin transport in lateral ferromagnet–semiconductor devices*, Nature Physics **3** (2007), no. 3, 197–202.

[65] R. Meservey and P. M. Tedrow, *Surface relaxation times of conduction-electron spins in superconductors and normal metals*, Physical Review Letters **41** (1978), no. 12, 805–808.

[66] G. X. Miao, K. S. Yoon, T. S. Santos, and J. S. Moodera, *Influence of spin-polarized current on superconductivity and the realization of large magnetoresistance*, Physical Review Letters **98** (2007), no. 26, 267001.

[67] Katsuya Miura, Shinya Kasai, Kensuke Kobayashi, and Teruo Ono, *Non local spin detection in ferromagnet/superconductor/ferromagnet spin-valve device with double-tunnel junctions*, Japanese Journal of Applied Physics **45** (2006), no. 4A, 2888–2891.

[68] T. Miyazaki and N. Tezuka, *Giant magnetic tunneling effect in fe/al2o3/fe junction*, Journal of Magnetism and Magnetic Materials **139** (1995), no. 3, L231 – L234.

[69] J. S. Moodera, *Large magnetoresistance at room temperature in ferromagnetic thin film tunnel junctions*, Physical Review Letters **74** (1995), no. 16, 3273–3276.

[70] M. Murat, Y. Gefen, and Y. Imry, *Ensemble and temperature averaging of quantum oscillations in normal-metal rings*, Physical Review B **34** (1986), no. 2, 659–668.

[71] D. A. Papaconstantopoulos, *Handbook of the band structure of elemental solids*, Plenum, New York, 1986.

[72] Stuart S. P. Parkin, Christian Kaiser, Alex Panchula, Philip M. Rice, Brian Hughes, Mahesh Samant, and See-Hun Yang, *Giant tunnelling magnetoresistance at room temperature with mgo (100) tunnel barriers*, Nature Materials **3** (2004), no. 12, 862–867.

[73] N. Poli, J. P. Morten, M. Urech, Arne Brataas, D. B. Haviland, and V. Korenivski, *Spin injection and relaxation in a mesoscopic superconductor*, Physical Review Letters **100** (2008), no. 13, 136601.

[74] J. W. A. Robinson, J. D. S. Witt, and M. G. Blamire, *Controlled injection of spin-triplet supercurrents into a strong ferromagnet*, Science **329** (2010), no. 5987, 59–61.

[75] J. Romijn, *Critical pair-breaking current in superconducting aluminum strips far below tc*, Physical Review B **26** (1982), no. 7, 3648–3655.

[76] Joseph Samuel, *General setting for berry's phase*, Physical Review Letters **60** (1988), no. 23, 2339–2342.

[77] Manfred Sigrist and Kazuo Ueda, *Phenomenological theory of unconventional superconductivity*, Reviews of Modern Physics **63** (1991), no. 2, 239–311.

[78] Jairo Sinova, *Spin hall effects*, Reviews of Modern Physics **87** (2015), no. 4, 1213–1260.

[79] Ady Stern, *Berry's phase, motive forces, and mesoscopic conductivity*, Physical Review Letters **68** (1992), no. 7, 1022–1025.

[80] Myron Strongin, O. F. Kammerer, and Arthur Paskin, *Superconducting transition temperature of thin films*, Physical Review Letters **14** (1965), no. 23, 949–951.

[81] D. Suter, *Study of the aharonov-anandan quantum phase by nmr interferometry*, Physical Review Letters **60** (1988), no. 13, 1218–1220.

[82] S. Takahashi and S. Maekawa, *Spin injection and detection in magnetic nanostructures*, Physical Review B **67** (2003), no. 5, 052409.

[83] P. M. Tedrow, *Spin-dependent tunneling into ferromagnetic nickel*, Physical Review Letters **26** (1971), no. 4, 192–195.

[84] Nikolaos Tombros, Csaba Jozsa, Mihaita Popinciuc, Harry T. Jonkman, and Bart J. van Wees, *Electronic spin transport and spin precession in single graphene layers at room temperature*, Nature **448** (2007), no. 7153, 571–574.

[85] Akira Tomita and Raymond Y. Chiao, *Observation of berry's topological phase by use of an optical fiber*, Physical Review Letters **57** (1986), no. 8, 937–940.

[86] Akira Tonomura, *Observation of aharonov-bohm effect by electron holography*, Physical Review Letters **48** (1982), no. 21, 1443–1446.

[87] C. P. Umbach, C. Van Haesendonck, R. B. Laibowitz, S. Washburn, and R. A. Webb, *Direct observation of ensemble averaging of the aharonov-bohm effect in normal-metal loops*, Physical Review Letters **56** (1986), no. 4, 386–389.

[88] A. F. Volkov, F. S. Bergeret, and K. B. Efetov, *Odd triplet superconductivity in superconductor-ferromagnet multilayered structures*, Physical Review Letters **90** (2003), no. 11, 117006.

[89] Jian Wang, Meenakshi Singh, Mingliang Tian, Nitesh Kumar, Bangzhi Liu, Chuntai Shi, J. K. Jain, Nitin Samrth, T. E. Mallouk, and M. H. W. Chan, *Interplay between superconductivity and ferromagnetism in crystalline nanowires*, Nature Physics **6** (2010), 389.

[90] Sean Washburn and Richard A. Webb, *Aharonov-bohm effect in normal metal quantum coherence and transport*, Advances in Physics **35** (1986), no. 4, 375–422.

[91] R. A. Webb, S. Washburn, C. P. Umbach, and R. B. Laibowitz, *Observation of h/e aharonov-bohm oscillations in normal-metal rings*, Physical Review Letters **54** (1985), 2696.

[92] John C. Wheatley, *Experimental properties of superfluid 3he*, Reviews of Modern Physics **47** (1975), no. 2, 415–470.

[93] Y. Yafet, *g factors and spin-lattice relaxation of conduction electrons*, Solid State Physics: Advances in Research and Applications (Frederick Seitz and David Turnbull, eds.), Solid State Physics, vol. 14, Academic Press, 1963, pp. 1 – 98.

[94] Y. S. Yi, T. Z. Qian, and Z. B. Su, *Spin precession and time-reversal symmetry breaking in quantum transport of electronsthrough mesoscopic rings*, Physical Review B **55** (1997), no. 16, 10631–10637.

[95] Shinji Yuasa, Taro Nagahama, Akio Fukushima, Yoshishige Suzuki, and Koji Ando, *Giant room-temperature magnetoresistance in single-crystal fe/mgo/fe magnetic tunnel junctions*, Nature Materials **3** (2004), no. 12, 868–871.

[96] Igor Žutić, Jaroslav Fabian, and S. Das Sarma, *Spintronics: Fundamentals and applications*, Reviews of Modern Physics **76** (2004), no. 2, 323–410.